Journal of Advanced Ceramics
2023, **12**(4): 649–680
https://doi.org/10.26599/JAC.2023.9220703
ISSN 2226-4108
CN 10-1154/TQ

Review

Multi-scale synergic optimization strategy for dielectric energy storage ceramics

Xuhui Fan[a,b,c], Jing Wang[a,*], Hao Yuan[a,b], Zehan Zheng[a,b], Ji Zhang[d,*], Kongjun Zhu[a,*]

[a]*State Key Laboratory of Mechanics and Control of Mechanical Structures, College of Aerospace Engineering, Nanjing University of Aeronautics and Astronautics, Nanjing 210016, China*
[b]*School of Materials Science and Engineering, Nanjing University of Aeronautics and Astronautics, Nanjing 210016, China*
[c]*Department of Materials Science and Engineering, Southern University of Science and Technology, Shenzhen 518055, China*
[d]*School of Materials Science and Engineering, Nanjing University of Science and Technology, Nanjing 210094, China*

Received: September 23, 2022; Revised: November 18, 2022; Accepted: December 3, 2022

Abstract: Dielectric capacitors, serving as the indispensable components in advanced high-power energy storage devices, have attracted ever-increasing attention with the rapid development of science and technology. Among various dielectric capacitors, ceramic capacitors with perovskite structures show unique advantages in actual application, e.g., excellent adaptability in high-temperature environments. And the optimization of their energy storage performance has become a hot research topic recently. This review presents the basic principles of energy storage in dielectric ceramics and introduces multi-scale synergic optimization strategies according to the key factors for superior energy storage performance. By summarizing the common points in numerous works, several universal modification strategies are reviewed, and future research on fatigue fracture of ceramic capacitors under multi-field including but not limited to force, electric, and thermal coupling conditions is also anticipated.

Keywords: dielectric capacitors; high-power; energy storage; multi-scale

1 Introduction

With the rapid development of economy and technology, the demand for energy is continually increasing. However, the over-exploitation of traditional fossil resources such as oil and coal has caused a series of problems such as resource depletion and environmental degradation. In accordance with The Paris Agreement, the global carbon neutrality targets will be achieved by 2030, and total carbon dioxide emissions will be reduced by ~45% [1,2]. Therefore, it is very urgent to develop the new clean energy sources

* Corresponding authors.
E-mail: J. Wang, wang-jing@nuaa.edu.cn;
J. Zhang, jizhang@njust.edu.cn;
K. Zhu, kjzhu@nuaa.edu.cn

(such as solar, wind, and geothermal). Although the development of renewable energy is encouraged in recent years, it is still limited by many barriers such as intermittent and geographical limitations. In order to get rid of the dependence on fossil fuels, it is necessary to study energy storage and conversion devices. There are mainly three kinds of electrical energy storage devices: batteries, electrochemical capacitors, and dielectric capacitors [2–5]. Compared with batteries and electrochemical capacitors, dielectric capacitors do not involve any chemical reaction during the energy storage and release, so the discharge speed is extremely fast. Figure 1(a) shows the characteristics of these energy storage devices. It is clear that dielectric capacitors reveal distinctive features of ultra-high power density (10^6–10^7 W/kg) and fast charge/discharge rate (microsecond or even nanosecond) [6–9]. Therefore, they are widely utilized in high-power and high-pulse fields, such as electric vehicles, power grids, aircraft, and radar (Fig. 1(b)). In addition, they possess the advantages of simple preparation, no liquid component, high working voltage, a wide range of temperatures, good safety performance, etc. [10,11].

The research on dielectric capacitor materials has been a hot topic recently. The current mainstream research directions are divided into three categories: polymer dielectrics, film capacitors, and ceramic counterparts. Due to the low dielectric constants of polymer dielectrics, the energy density is badly limited. For example, the dielectric constant of biaxially oriented polypropylene (BOPP) is around 2.2, and the corresponding capacitors usually exhibit the small energy no more than 5 J/cm^3 [11,12]. The film capacitors generally show ultra-high energy density, but the total energy is quite low because of the limited volume [13,14]. Ceramic capacitors usually have high relative dielectric constant (ε_r) up to 10^3. For example, the ε_r of $BaTiO_3$ (BT)-based X7R-type ceramics can reach as high as 2000 [2,15]. Ceramic capacitors with large dielectric constants display great potential for energy storage performance. However, the limited breakdown strength hinders their further increment of energy density. Therefore, stabilizing the dielectric constant while improving the electric breakdown strength (E_b) is of great importance for the ceramic capacitors.

In the present review, we introduce the principles of energy storage performance of ceramic capacitors, including the characteristics and influencing factors. Next, we list the current general strategies and methods to optimize the energy storage performance of ceramic capacitors. Finally, we summarize the optimal strategy for ceramic capacitors with high performance and look forward to the future development of ceramic capacitors.

2 Principle of energy storage of capacitors

2. 1 Energy storage and release

The energy storage of dielectric capacitor is based on the polarization (P) of internal dipoles upon applying the external electric field. Energy is stored and released in the process of polarization and depolarization, as shown in Fig. 2(a) [16,17]. Since no redox reaction or material transfer occurs during the whole process, the accumulated energy during charging process can be released quickly, generating a strong electrical pulse

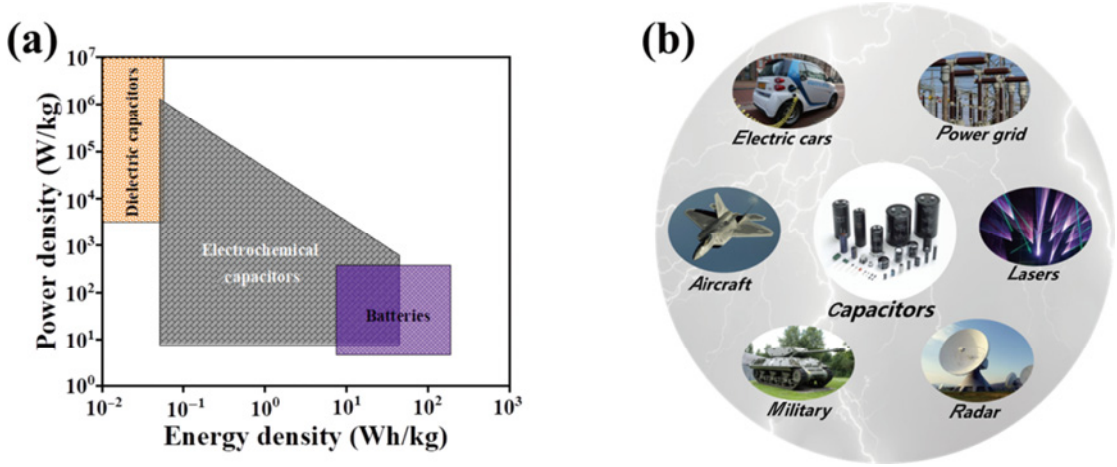

Fig. 1 (a) Comparison of power density and energy density capabilities of dielectric capacitors, electrochemical capacitors, and batteries [9]. (b) Applications for dielectric capacitors [2,11,25].

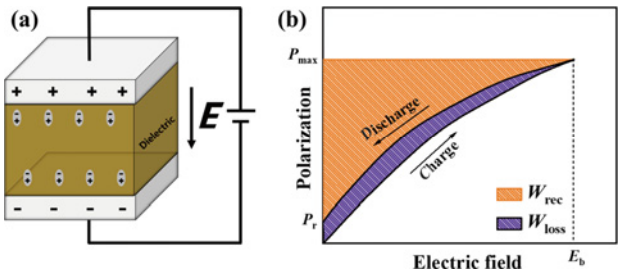

Fig. 2 (a) Circuit diagram of parallel plate dielectric capacitor. (b) Recoverable energy density (W_{rec}) and energy storage loss (W_{loss}) [17].

[11,16]. The energy stored per unit volume (i.e., charged energy density (W_{st})) is expressed by Eq. (1):

$$W_{st} = \frac{W}{Ad} = \frac{\int_0^{Q_{max}} V\mathrm{d}Q}{Ad} = \int_0^{D_{max}} E\mathrm{d}D \quad (1)$$

where A is the electrode area of capacitor, d is the thickness, W is the total energy stored in the dielectric capacitor, and V, Q, Q_{max}, E, D, and D_{max} represent the applied voltage, accumulated charge, maximum accumulated charge, applied electric field, electric displacement, and maximum electric displacement, respectively [8].

The D in dielectric materials is closely related to the polarization ($D = P + \varepsilon_0 E$), while for high dielectric constant materials, D is approximately equal to $P = \varepsilon_0\varepsilon_r E$ (ε_0 is the vacuum dielectric constant). For linear dielectric (LD) materials, the dielectric constant does not vary with the applied electric field, and W_{st} can be expressed by Eq. (2):

$$W_{st} = \int_0^{D_{max}} E\mathrm{d}D = \frac{1}{2}\varepsilon_0\varepsilon_r E^2 \quad (2)$$

For nonlinear dielectric materials, certain energy dissipation is exhibited during the charging and discharging due to the polarization hysteresis. W_{st} and W_{rec} can be obtained by integrating the integral area of the hysteresis line separately, as shown in Fig. 2(b) [18–20].

$$W_{st} = \int_0^{P_{max}} E\mathrm{d}P \quad (3)$$

$$W_{rec} = \int_{P_r}^{P_{max}} E\mathrm{d}P \quad (4)$$

$$W_{st} = W_{rec} + W_{loss} \quad (5)$$

$$\eta = \frac{W_{rec}}{W_{st}} \times 100\% \quad (6)$$

where P_{max} and P_r denote the maximum polarization and the residual polarization, respectively, and η is the energy efficiency. For dielectric materials, the main parameters to evaluate the energy storage capacity include W_{rec} and η. Therefore, it can be seen from Eq. (4) that dielectric materials with high P_{max}, low P_r, and high E_b are more valuable for applications of energy storage.

The E_b of ceramic capacitors is affected by a variety of factors, including but not limited to relative density, ceramic thickness, grain size, resistivity, type of test voltage, and temperature [21–24]. It is found that the E_b of ceramic capacitors can be improved by more than several times by reducing the thickness of ceramics because of the reduction in the probability of defects [23,25,26]. Moreover, a second phase cladding layer with low dielectric constants on ceramic grains is also effective to enhance E_b [21,27,28]. In addition, adjusting the fabrication process to decrease the grain size, modifying the ceramics to reduce the ionic conductivity, and boosting band gap (E_g) to prevent the electronic transition are of great significance to improve E_b of ceramic capacitors [27–29]. As the polarization modulation, P_{max} is related to the material features and vacancies, while P_r can be optimized by resizing the domains [30–35].

2. 2 Dielectric materials for energy storage capacitors

Dielectric materials for energy storage capacitors are usually classified into different categories according to their hysteresis loops, namely LDs, ferroelectrics (FEs), relaxor ferroelectrics (RFEs), and antiferroelectrics (AFEs). The related polarization–specific electric field behavior (i.e., P–E loop) and domain structures are shown in Fig. 3 [2,8,25].

Theoretically, the dielectric constant of LDs does not vary with the electric field, and thus exhibits the near-linear characteristic, as shown in Fig. 3(a). These materials are usually characterized by high E_b, low dielectric loss, and low P_{max}. The widely studied LD materials include TiO_2, $CaTiO_3$, and $SrTiO_3$ (ST) [36–38].

FEs normally reveal large P_{max} and high dielectric constants [39]. When the electric field is applied, the FE domains respond to the electric field, while the FE domains partly go back to their original states upon removing the electric field. Figure 3(b) displays the typical hysteresis P–E loops of FEs. The energy storage density of FEs is low due to the large P_r. Therefore, they usually serve as the fillers to the glass- or polymer-matrix to enhance the dielectric constants [40–43].

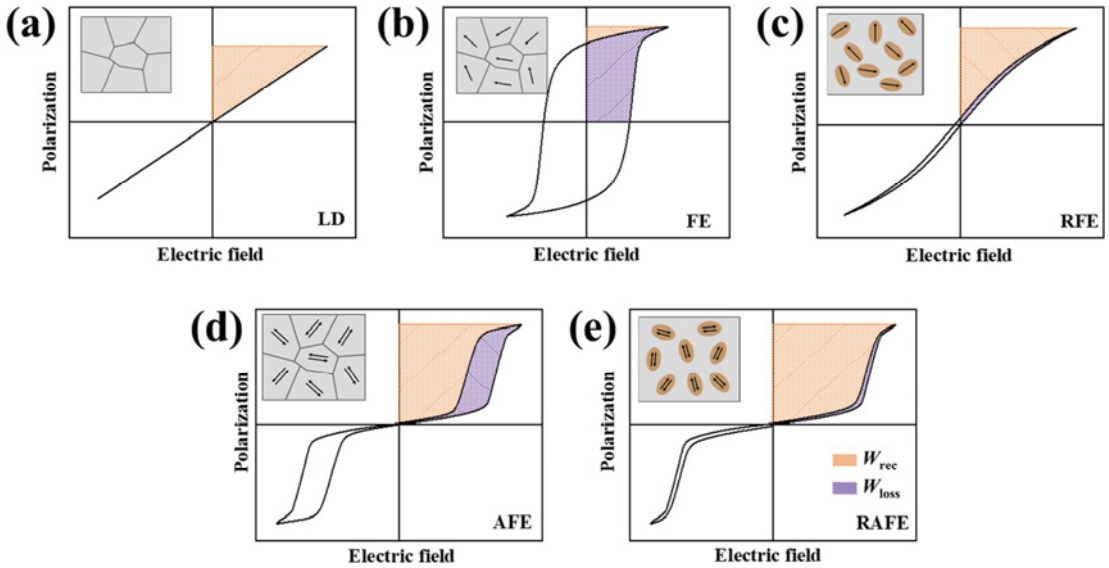

Fig. 3 Typical *P*–*E* loops of (a) LDs, (b) FEs, (c) RFEs, (d) AFEs, and (e) RAFEs [2,11].

Different from the FEs with long-range FE orders, the RFEs generally exhibit short-ranged FE orders with high P_{max}, low P_r, high dielectric constants, and slim *P*–*E* curves, as shown in Fig. 3(c). These features do favor to the excellent energy storage performance [44]. After the RFE was first discovered in the BT–$BaSnO_3$ system in 1954, most research focuses on Pb-based systems and lead-free Bi-based systems [45].

In AFEs, dipoles tend to arrange in pairs in the opposite directions, and therefore do not show polarity macroscopically [45,46]. When they are subjected to an external electric field, the AFE–FE phase transition will occur and give rise to a jump in polarization. When the applied electric field is switched off, it will revert from FE to AFE again. The *P*–*E* curve exhibits the characteristics of a double hysteresis loop, as shown in Fig. 3(d). The present research of AFE materials are mainly concentrated on the systems of (Pb,La)$(Zr,Ti)O_3$, $AgNbO_3$ (AN), $NaNbO_3$ (NN), $(Bi,Na)TiO_3$ (BNT), etc. [34,47–51].

RAFEs are normally regarded as a special kind of AFE materials. Due to the disturbance of macro AFE orders and emergence of nanodomains with weak couplings, they usually tend to exhibit *P*–*E* curves with suppressed hysteresis, which is very different from typical AFEs. Thus, RAFEs show great potential in energy storage with the synergistic optimization of W_{rec} and η. The present research on RAFEs is mainly focused on AN-, BNT-, and NN-based systems [52–54].

Although dielectric materials have their advantages in terms of energy storage, the energy density of ceramic materials is generally no more than 2 J/cm^3 due to limited dielectric constant, low E_b, or high dielectric loss [38,55,56]. The dielectric capacitors with high W_{rec} and energy efficiency should not only possess high dielectric constants and high E_b, but also require low dielectric loss and fast dielectric response, which are the main stream of present optimization of dielectric capacitors. Selecting appropriate ceramic materials and optimization methods is the key to improving the energy storage performance of dielectric capacitors.

3 Improvement strategies for energy storage performance

The ceramic capacitor is an energy storage device with a multi-scale structure, which exhibits different characteristics at different scales, as shown in Fig. 4. So, there are many methods to optimize the energy storage performance [57–59].

At the nanoscale, doping is often used to improve the intrinsic E_g, reduce the ion mobility, or enhance the conductive activation energy (E_a), which is of great significance for large voltage tolerance [47,60–62]. Furthermore, doping can also affect phase structures and domain structures, which is an indispensable modification method for phase engineering and domain engineering [32,52,54,63–65].

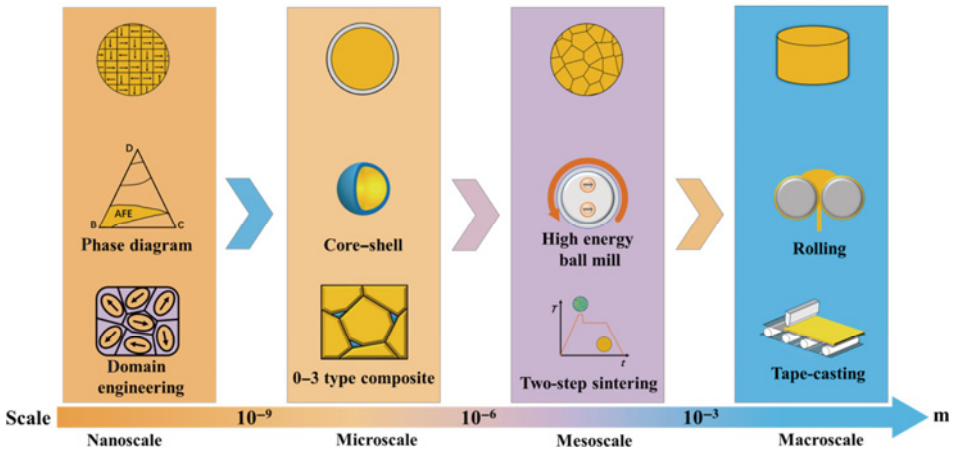

Fig. 4 Structures and optimization strategies of ceramic capacitors at different scales.

At the microscale, constructing the core–shell structure and composite structure are two of the important ways to enhance the energy storage performance of ceramic capacitors [27,28,66–70]. For example, the dielectrics with a high E_b (e.g., SiO_2) can be deposited on the surface of the FE materials with high polarization, which would enhance the apparent E_b of dielectric materials while retaining the high polarization [28,71]. The addition of insulating metallic oxide (such as ZnO, MgO, and Al_2O_3) will precipitate at the grain boundary to prevent ceramic broken down, and then enhance their E_b values [69,70,72].

At the mesoscale, reducing the grain size to improve the E_b is one of the most common modified methods. On the one hand, the reduction of the grain size increases the content of grain boundaries with high resistivity, which improves the dielectric breakdown resistance. On the other hand, the breakdown path of the electrical tree is more complex in fine-grained ceramics, and dielectric breakdown requires higher energy [22,73–75].

At the macroscale, the tape-casting and rolling process are two effective methods. The bulk ceramics prepared via the traditional solid-state reaction usually contain many defects and reveal low relative density, resulting in low E_b [76]. Multilayer ceramic capacitors (MLCCs) prepared via the tape-casting process can simultaneously increase the relative density and reduce the thickness of single-layer ceramics to greatly enhance E_b. The multilayer stacking also enables the miniaturization and integration of ceramic capacitors [23,34,57,58]. The rolling process involves pouring the mixture of ceramic powders and polyvinyl alcohol (PVA) into a roller, which is extruded and shaped to obtain high-density ceramics. The whole preparation process is simple and suitable for industrial production [77,78].

It is reported that more than two modification strategies are often used together to enhance the energy storage performance. The modification methods at different scales have their own characteristics, and multi-scale collaborative optimization can improve the all-around performance of capacitors.

3. 1 Nanoscale modification

The materials with perovskite structures (ABO_3) for dielectric energy storage are the most widely investigated. The doping elements can be divided into A- and/or B-site doping according to the occupied position [34,63,79,80]. First, the ionic radius should be well chosen. On the one hand, the ionic radius of doping elements should be different from that of the element in the corresponding position to induce lattice distortions; on the other hand, too large radius differences between doping and host elements would result in the failure of doping. Second, the ionic valence states of them do not differ too much to avoid charge imbalance. Third, the substituted element cannot react with the A-/B-site elements to form the second phase or impurity. Doping is an effective mean of ceramic modification via phase engineering [33,52,81–83], domain engineering [32,64], and manipulating breakdown and polarization [47,61,62,84,85].

3.1.1 Phase engineering

Dielectric ceramics have abundant phase transitions. In some cases, the room-temperature phase structure is not conducive to energy storage [33,52]. Therefore, the construction of target phase regions via doping is a

valid and effective modification method to optimize the energy storage performance.

Lead-based AFE ceramics are widely used in the field of high power/pulses due to their excellent W_{rec} and η. The current research hotspots mainly include $Pb(Zr,Ti)O_3$ (PZT) [86], $(Pb,La)(Zr,Ti)O_3$ [81,87–89], $(Pb,La)(Zr,Sn,Ti)O_3$ [90–93], and $(Pb,La)(Zr,Sn)O_3$ [48,94].

PZT is a binary solid solution of $PbZrO_3$ (PZO) and $PbTiO_3$. As shown in Fig. 5(a), PZT ceramics exhibit antiferroelectricity when the doping content of Ti^{4+} is within 0–5 mol% [86]. Interestingly, when La^{3+} and Sn^{4+} are introduced, the doping content of Ti^{4+} can be increased from 5 to 10 mol% (Fig. 5(b)). In other words, the AFE phase region is expanded, providing more possibilities for the design of lead-based AFE materials [82,83].

PZT-based AFE ceramics have great potential for energy storage applications, but its energy efficiency is very limited due to large hysteresis induced by the phase transition [56]. A relaxation behavior is successfully constructed near the phase boundary by doping La^{3+} (Fig. 5(c)), which effectively disrupts the long-range AFE orders, generates polar nanoclusters, and finally exhibits elongated electrical hysteresis curves (Fig. 5(d)). Moreover, La^{3+} can also stabilize the AFE phase near the AFE–FE grain boundary [81,95–98]. The energy density of 3.04 J/cm^3 with an energy efficiency of 92% is realized in PLZT ceramics [81]. Due to the improved energy efficiency, the energy consumed in the form of heat during the cycling process is obviously reduced. The reliability is thus improved, and the performance remains unchanged after 10,000 cycles [81]. Zhang *et al*. [95] reported that the room-temperature phase changes from orthogonal AFE (AFE_O) to tetragonal AFE (AFE_T) after introducing Sr^{2+} into the $(Pb_{0.97}La_{0.02})(Zr_{0.75}Sn_{0.195}Ti_{0.055})O_3$ system. Meanwhile, the stability of the AFE phase increases simultaneously. The energy density increases from 3.53 to 5.56 J/cm^3 as the doping content goes up to 1.5 mol%. Benefiting from the expansion of temperature region of the AFE phase, the energy density varies less than 12% in the temperature range of 30–90 ℃ [56,95].

Pb-based ceramics display a variety of phase regions, and thus reveal many possibilities to improve the energy storage capacity by adjusting the phase structure. Taking the $(Pb_{1-1.5x}La_x)(Zr_{0.66}Sn_{0.23}Ti_{0.11})O_3$ (PLZST)

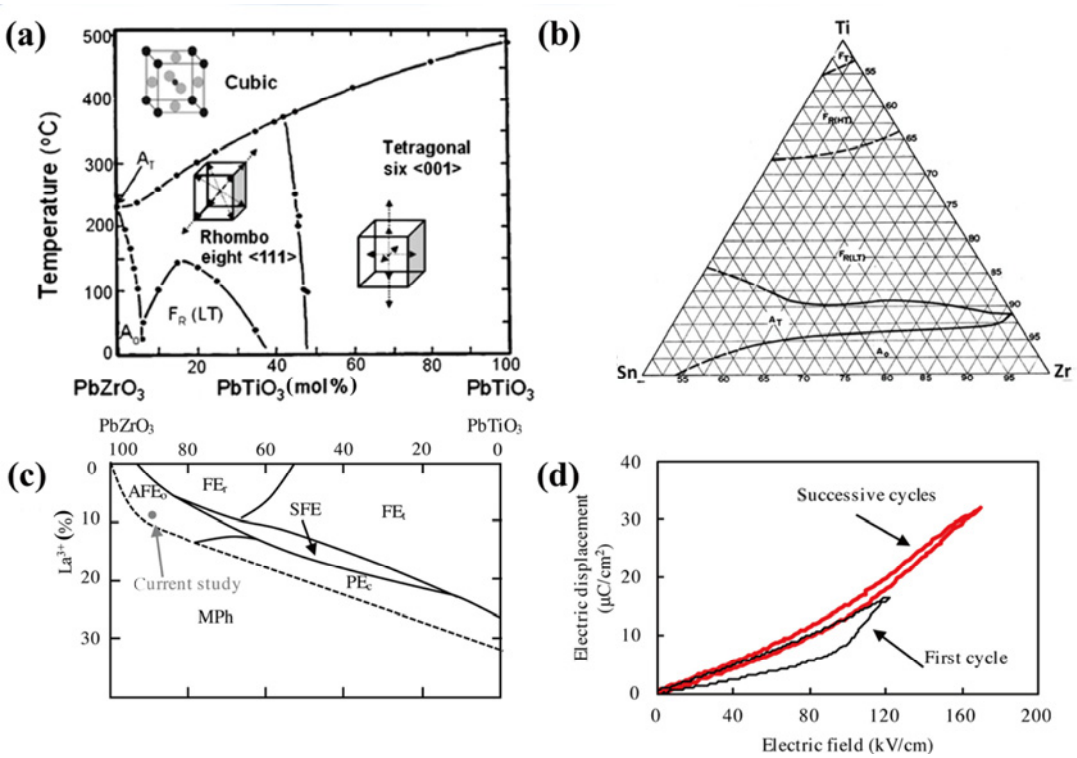

Fig. 5 Phase diagrams of (a) PZO–$PbTiO_3$ and (b) $(Pb_{0.97}La_{0.02})(Zr,Sn,Ti)O_3$. (c) Phase diagram and (d) energy storage performance of $(Pb_{0.88}La_{0.08})(Zr_{0.91}Ti_{0.09})O_3$ (PLZT). Reproduced with permission from Ref. [86] for (a), © Springer Nature 2007; Ref. [82] for (b), © WILEY-VCH Verlag GmbH & Co. KGaA, Weinheim 2018; Ref. [81] for (c, d), © AIP Publishing LLC 2016.

ceramics for instance, when the content of La^{3+} exceeds 2 mol%, PLZST ceramic systems undergo an FE–AFE phase transition. As the content of La^{3+} is increased to 4 mol%, the energy density changes from ~0.1 to ~1.47 J/cm^3 in PLZST ceramics [99]. In addition to the La^{3+} content, the phase structure of PLZST ceramics can also be manipulated by changing the ratios of Zr, Sn, and Ti, as shown in Table 1.

The phase engineering of lead-free systems can be also efficiently designed and modulated via the atomic doping. AN is an AFE material with perovskite structures. Fu *et al*. [55] reported that AN undergoes an AFE–FE phase transition when the applied electric field exceeds 180 kV/cm and produces a large P_{max} of ~52 μC/cm^2, as shown in Fig. 6(a). At room temperature (RT), AN is the ferrielectric M_1 phase and exhibits ferrielectric properties that are not favorable for energy storage [102,103]. As the temperature rises, the phase structure gradually transforms into disordered AFE M_2 and M_3 phases, as shown in Fig. 6(b). Zhao *et al*. [34] found that the replacement of Nb^{5+} by Ta^{5+} with lower polarizability enhances the antiferroelectricity of AN, so that the disordered AFE M_2 phase can be successfully stabilized at RT (Fig. 6(c)). When the content of Ta^{5+} is 15 mol%, the energy density and energy efficiency can be enhanced to ~4.2 J/cm^3 and ~69%, respectively (Figs. 6(d) and 6(e)).

Since Ta^{5+} (0.64 Å, coordination number (CN) = 6) and Nb^{5+} (0.64 Å, CN = 6) have the same ionic radius and valence state, AN and $AgTaO_3$ (AT) have the infinite miscibility [104]. Luo *et al*. [52] successfully implemented the design of relaxor AFE at the M_2–M_3 phase boundary by adjusting the ratio of Nb to Ta in the AN–AT solid solution. As the Ta^{5+} content increases, the M_2–M_3 phase boundary is gradually stabilized at RT. Meanwhile, the *P*–*E* loops become slanted and slim. The obtained 0.45AN–0.55AT ceramics show the further enhanced W_{rec} of 6.3 J/cm^3 and η of 90% at 470 kV/cm.

The phase structure modulation of AN can be also achieved by introducing A-site doping, such as La^{3+}, Sm^{3+}, Nd^{3+}, Gd^{3+}, and Sr^{2+} [65,105–108]. The substitution of La^{3+} (1.36 Å, CN = 12) with a smaller ionic radius than Ag^+ (1.48 Å, CN = 12) in the A-site of AN leads to lattice shrinkage, reduction in the lattice distortion, and enhancement in symmetry. The increment in the AFE phase stability is thus obtained [52,109]. The room-temperature phase structure of AN gradually changes from the FE M_1 phase to the AFE

Table 1 Energy storage performance of PLZST ceramics with different ratios of Zr, Sn, and Ti

Composition	E_b (kV/cm)	W_{rec} (J/cm^3)	η (%)	Ref.
$Pb_{0.97}La_{0.02}(Zr_{0.58}Sn_{0.35}Ti_{0.07})O_3$	118	2.35	86.1	[100]
$Pb_{0.97}La_{0.02}(Zr_{0.50}Sn_{0.46}Ti_{0.04})O_3$	150	3.2	86.5	[93]
$Pb_{0.97}La_{0.02}(Zr_{0.56}Sn_{0.35}Ti_{0.09})O_3$	175	3.3	80	[101]
$Pb_{0.97}La_{0.02}(Zr_{0.60}Sn_{0.35}Ti_{0.05})O_3$	200	4.1	—	[92]
$Pb_{0.97}La_{0.02}(Zr_{0.5}Sn_{0.44}Ti_{0.06})O_3$	250	4.2	82	[91]
$Pb_{0.97}La_{0.02}(Zr_{0.5}Sn_{0.45}Ti_{0.05})O_3$	400	5.6	63	[90]

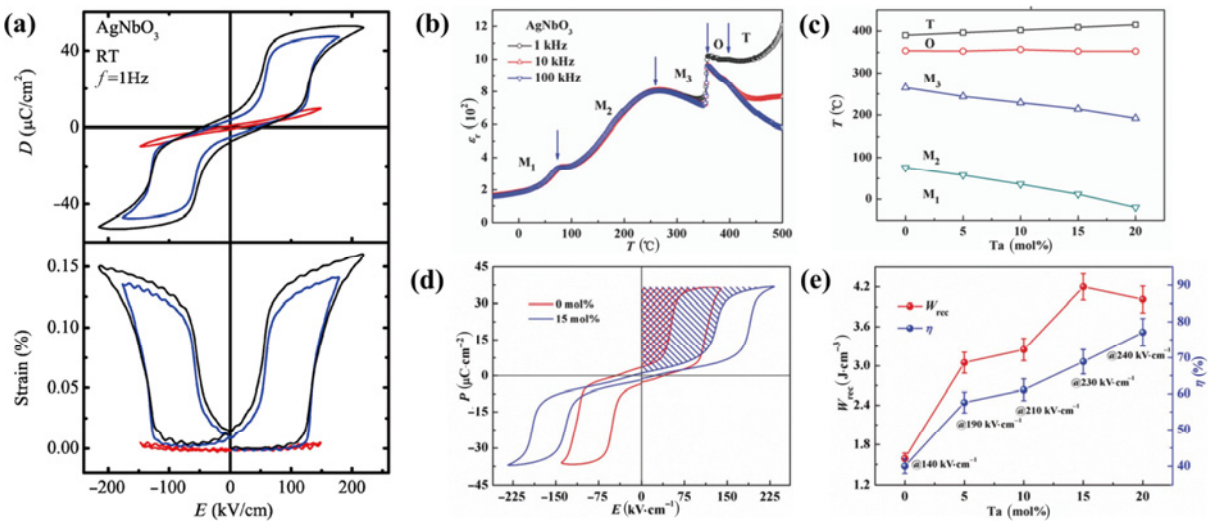

Fig. 6 (a) *D*–*E* and strain–*E* loops of AN ceramics, where *f* is the frequency. (b) Temperature (*T*) and ε_r dependence of dielectric constants of AN ceramics. (c) Phase diagram of $AgNb_{1-x}Ta_xO_3$ ceramics. (d) *P*–*E* loops of AN and $AgNb_{0.85}Ta_{0.15}O_3$ (ANT) ceramics. (e) Energy storage performance of $AgNb_{1-x}Ta_xO_3$ ceramics. Reproduced with permission from Ref. [55] for (a), © American Institute of Physics 2007; Ref. [34] for (b–e), © WILEY-VCH Verlag GmbH & Co. KGaA, Weinheim 2017.

M_2 phase after the doping of La^{3+} for Ag^+ [105]. The AFE feature is more pronouncedly demonstrated by the enhanced electric field of AFE–FE/FE–AFE phase transition (E_A/E_F). As a result, the energy density reaches 3.12 J/cm^3 at 230 kV/cm in $Ag_{0.94}La_{0.02}NbO_3$ ceramics. Based on the same mechanism, Sm^{3+} (1.24 Å, CN = 12) with a much smaller ionic radius than La^{3+} is also introduced to AN to replace Ag^+. It is found that Sm^{3+} has a more intense effect on the AN phase structure at RT, which completely transforms into the M_2 phase with a higher energy density (> 3.5 J/cm^3). With the optimized Sm^{3+} content of 3 mol%, the $Ag_{0.91}Sm_{0.03}NbO_3$ ceramics has an enhanced energy density up to 5.2 J/cm^3 at 290 kV/cm [65]. Moreover, Li *et al*. [107] and Mao *et al*. [110] also successfully achieved the construction of AN phase engineering by doping Gd^{3+} and Lu^{3+} with the energy densities of 4.5 and 3.5 J/cm^3, respectively.

(K,Na)NbO_3 (KNN) is a binary solid solution of FE $KNbO_3$ and AFE NN. It possesses the strong FE characteristics with high P_{max} of ~50 μC/cm^2 [111]. However, the application of KNN in energy storage is badly limited due to its low E_b and large hysteresis [112]. KNN exhibits a series of phase transitions of rhombohedral–orthorhombic–tetragonal–cubic (R–O–T–C) with the rising temperature, as shown in Fig. 7(a). Chen *et al*. [33] introduced many special ions (Li^+, Ba^{2+}, Bi^{3+}, Sc^{3+}, Hf^{4+}, Zr^{4+}, Ta^{5+}, and Sb^{5+}) into the KNN ceramics to tailor T_{R-O}, T_{O-T}, T_{T-C}, and locally R–O–T–C multiphase nanoclusters (Fig. 7(b)). The R–O–T–C multiple phases can be directly observed in high-entropy KNN (KNN-H) ceramics by using atomic-resolution scanning transmission electron microscopy (STEM). The large number of polar nano-regions (PNRs) of ~1–3 nm can disrupt the long-range orders of the system, enhance the external electric field response rate of KNN-H ceramics, and thus improve the energy efficiency (Fig. 7(c)) [113]. A giant W_{rec} of ~10.06 J/cm^3 with ultra-high η of ~90.8% is successfully achieved in KNN-H ceramics (Fig. 7(d)).

In other lead-free systems, such as $BiFO_3$ (BF), BNT, and NN ceramics, the phase structure construction is also frequently used to improve the energy density and energy efficiency. For example, W_{rec} of ~2.21 J/cm^3 and η of ~76% are realized in BF-based ceramics by constructing mixed phases of *R*3*c* rhombohedral and *Pbnm* orthorhombic phase [114,115]. Qi and Zuo [53] obtained a W_{rec} of 7.02 J/cm^3 with η of 85% by introducing NN components into BNT ceramics to stabilize the AFE phase at RT.

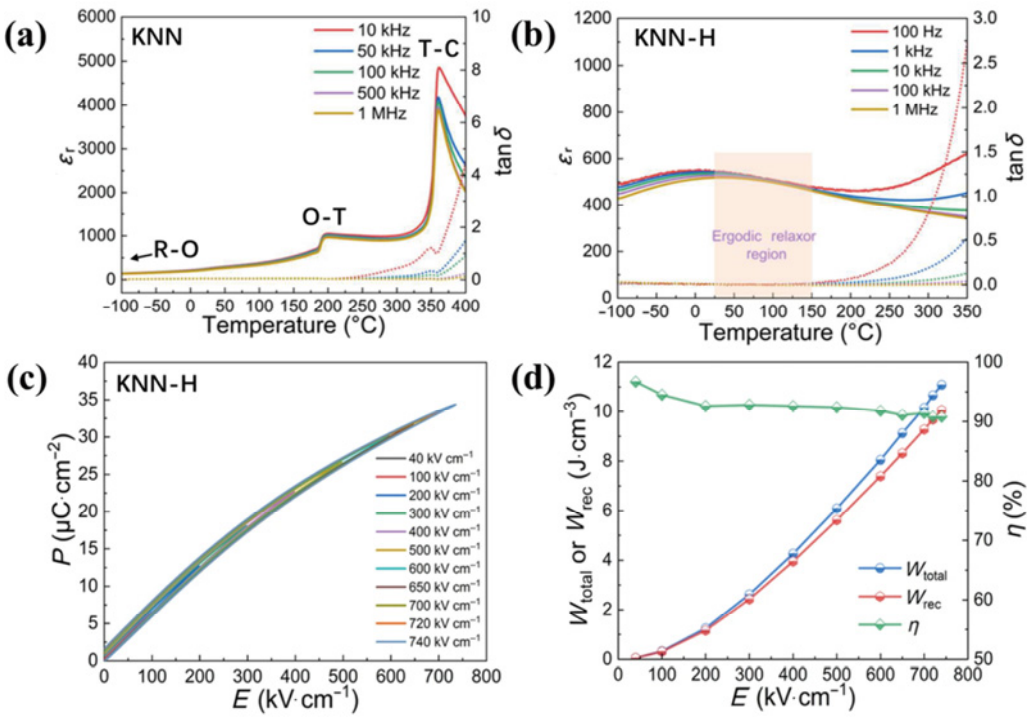

Fig. 7 Dielectric performance of (a) KNN and (b) KNN-H ceramics. (c) *P*–*E* loops and (d) energy storage performance of KNN-H ceramics. Reproduced with permission from Ref. [33], © The Author(s) 2022.

3.1.2 Domain engineering

High energy efficiency is one of the key indexes to evaluating the performance of ceramic capacitors. The low efficiency means large energy loss during the charge/discharge process. The energy loss of ceramic capacitors will be released in the form of thermal or mechanical energy, which will seriously deteriorate the electric breakdown of capacitors and limit their reliability in practice. The design of domain size and structures is very effective to enhance the energy efficiency. In ceramic materials, the nanodomains with weak couplings are very sensitive to the external electric field, so ceramic capacitors with a large number of nanodomains or PNRs tend to show slim *P–E* curves, accompanied by very small energy loss [29,32,47,64,116].

As AFE materials with the first order AFE–FE phase transition, AN is prone to showing large hysteresis during the transition process, which badly harms its energy storage efficiency [52]. Therefore, many research groups have spared no effort to construct nanodomains in AN ceramics to improve the energy efficiency. It is reported that the size of AFE domains can be reduced to less than 100 nm by substituting La^{3+} for Ag^{+} in AN ceramics [63]. The introduction of La^{3+} interrupts the long-range AFE orders, gives rise to nanodomains, and finally enhances η [63]. As shown in Fig. 8(a), well-ordered lamellar AFE microdomains and a large domain wall density can be observed in

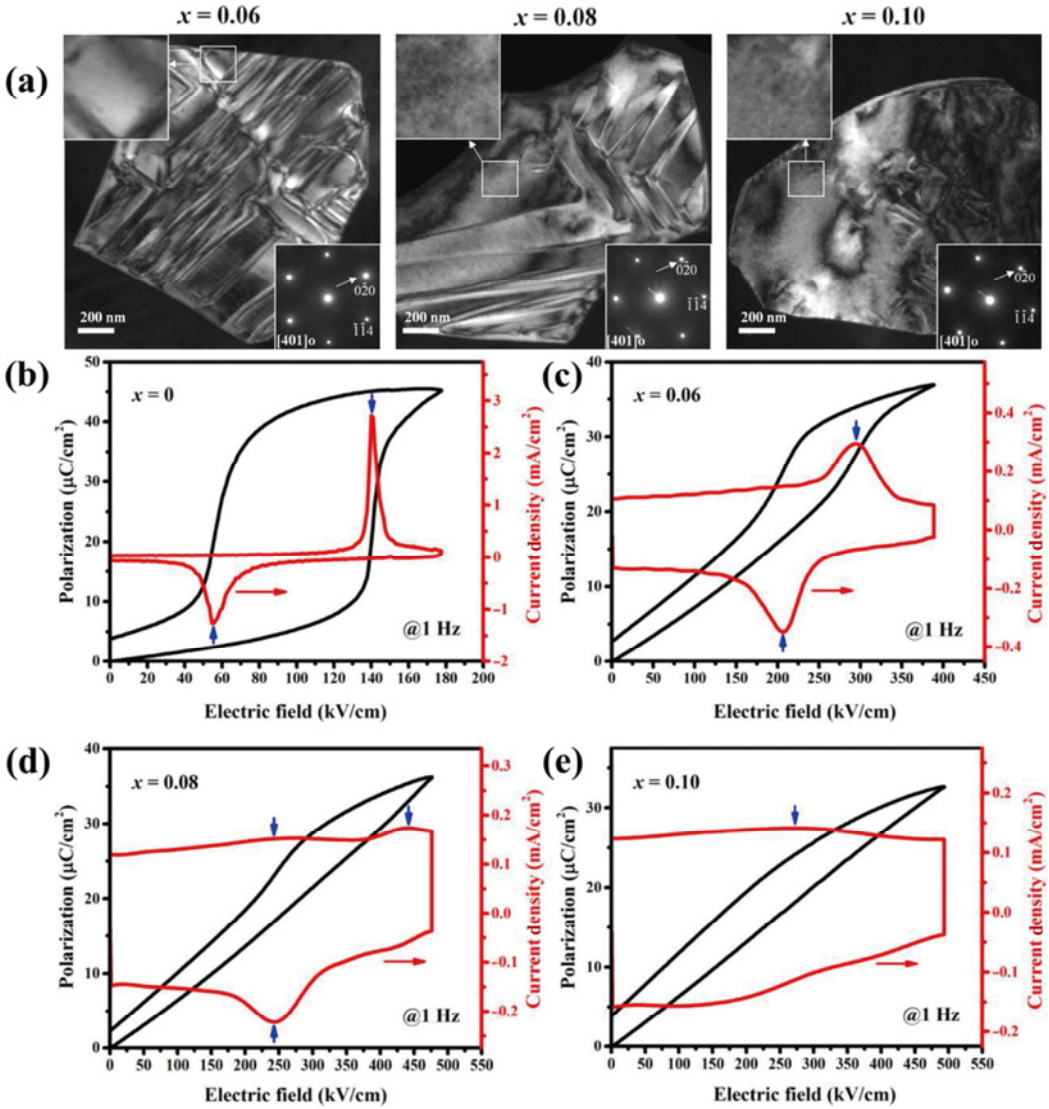

Fig. 8 (a) Dark-field TEM micrographs of ALN(x) ceramics along the orthorhombic [401] zone axis; the insets are the corresponding selected area electron diffraction patterns and the dark-field TEM image used the reflection that the arrows mark. (b–e) *P–E* and current density (*I*)–*E* loops of ALN(x) ceramics. Reproduced with permission from Ref. [63], © Elsevier B.V. 2020.

$Ag_{0.82}La_{0.06}NbO_3$ (ALN(0.06)) ceramic grains [117]. With the increasing La^{3+}, nano-sized AFE domains gradually appear, and the coexistence of micron and nano-sized AFE domains can be observed in ALN(0.08) ceramics. Nanodomains finally dominate with the further increment of La^{3+} (ALN(0.10)). Together with the change in domain size, the variation of *P*–*E* curves also occurs (Figs. 8(b)–8(e)). Because the nanodomains respond rapidly to the external electric field, the *P*–*E* curves of ceramics with La^{3+} doping appear to be more "slender" than those of pure AN ceramics. Moreover, La^{3+} also stabilizes the AFE stability of ceramics. The W_{rec} and η are 7.01 J/cm^3 and 77% at 476 kV/cm in ALN(0.10) [63], respectively.

Utilizing Nd^{3+} to replace Ag^+ on the A-site of AN ceramics can also reduce the domain sizes. The doping of Ag^+ by Nd^{3+} produces $Nd_{Ag}^{\cdot\cdot}$, which disrupts the antipolar orders and leads to a decrement in domain size. The domain width decreases from ~1 to < 0.3 μm when the content of Nd^{3+} increases to 3 mol%. The *P*–*E* curves change from square-shape with large hysteresis to the slim ones with low hysteresis after the co-doping of Nd^{3+} and Ta^{5+}. In addition, the introduction of Ta^{5+} stabilizes the antiferroelectricity, so that the $Ag_{0.97}Nd_{0.01}Ta_{0.20}Nb_{0.80}O_3$ ceramics exhibit large phase transition electric fields and achieve the W_{rec} of 6.5 J/cm^3 and η of 71% at 370 kV/cm. Similarly, Shi *et al*. [106] also observed AFE domains of 50–100 nm size in 1% Nd-doped AN ceramics and obtained W_{rec} of ~4.6 J/cm^3 and η of ~62.5%. Gao *et al*. [118] constructed AFE domains with a width of ~150 nm in $Ag_{0.91}Sm_{0.03}NbO_3$ ceramics and successfully upgraded W_{rec} and η to 4.3 J/cm^3 and 66%, respectively. Beside the rare earth elements, Sr^{2+} and Zn^{2+} are also utilized to build nanodomains in AN ceramics [108,119].

BT is a typical FE material with strong spontaneous polarization. And the large P_r and hysteresis greatly limit the energy storage properties, especially for η. Therefore, the construction of PNRs is a common modification method to enhance the energy efficiency [28,32,64,66]. Yuan *et al*. [32] reported the transition of BT from normal FEs to highly diffused and dispersed RFEs after incorporating $Bi(Mg_{0.5}Zr_{0.5})O_3$ (BMZ), accompanied by the generation of PNRs. As BMZ increases up to 5 mol%, the microstructures change from ordered lamellar domains (100 nm in width, Fig. 9(a)) to miniaturized lamellar domains (20–30 nm in width, Fig. 9(b)) surrounded by PNRs. With the further increment of BMZ, the FE domains gradually decrease, and PNRs gradually occupy the whole view (Fig. 9(c)). Since PNRs respond quickly to the applied electric field, the slim *P*–*E* loops with a suppressed hysteresis are obtained in Fig. 9(d). Finally, the W_{rec} of 2.9 J/cm^3 and η of 86.8% are achieved in BT–BMZ ceramics (Fig. 9(e)).

In 2021, Dai *et al*. [64] constructed PNRs in

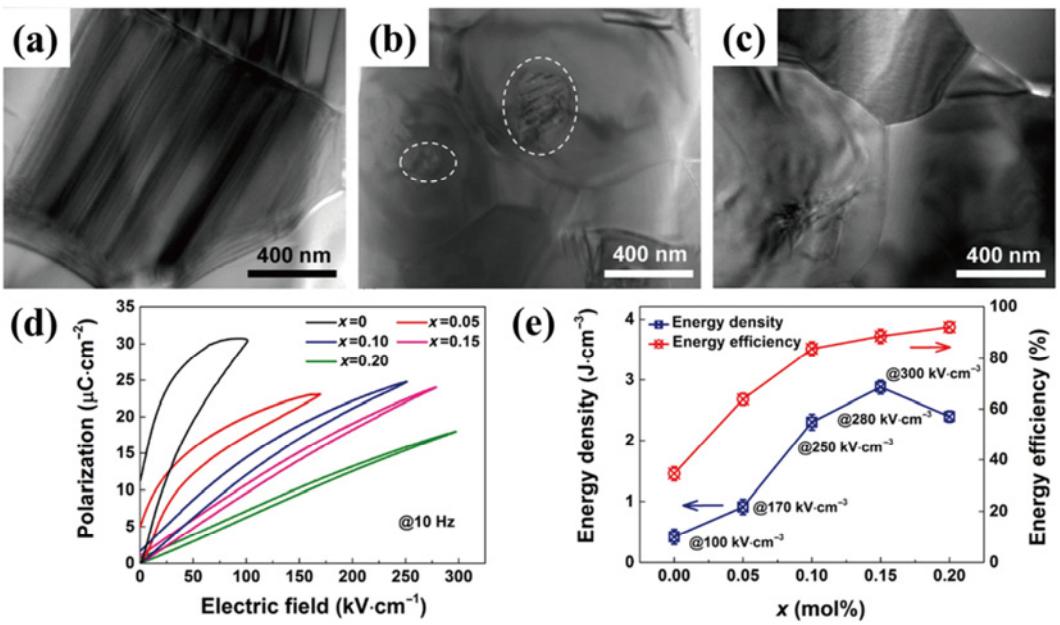

Fig. 9 Bright-field TEM micrographs of (1−*x*)BT–*x*BMZ ceramics for (a) *x* = 0, (b) *x* = 0.05, and (c) *x* = 0.15. (d) *P*–*E* loops and (e) energy storage performance of (1−*x*)BT–*x*BMZ ceramics. Reproduced with permission from Ref. [32], © Elsevier Ltd. 2018.

$Ba_{0.85}Ca_{0.15}Zr_{0.1}Ti_{0.9}O_3$ (BCZT) by introducing $Bi(Mg_{2/3}Nb_{1/3})O_3$ (BMN), which can effectively alleviate the hysteresis and eventually facilitate the ultra-high η of ~90.5% and W_{rec} of ~3.81 J/cm^3. When the applied electric field is switched off, the well-ordered FE domains cannot return to their initial states, which is the main reason for the low energy density and energy efficiency of BCZT ceramics. After the introduction of BMN, the long-range ordered structures are interrupted, and nanodomains appear. They can quickly return to the initial state upon the removing of applied electric field, which leads to low hysteresis and low P_r. A large number of highly dynamic polar nanodomains were constructed in $(Bi_{0.5}Na_{0.5})_{0.65}Sr_{0.35}TiO_3$ (BNST) ceramics via introducing BMZ. The long-range ordered polarities and the early polarization saturation were efficiently suppressed. With the help of refined grains and compact structure, 0.9BNST–0.1BMZ ceramic revealed a high E_b up to 522 kV/cm, the large W_{rec} of 8.46 J/cm^3 and η of 85.9% [120].

3.1.3 Breakdown and polarization

In dielectric energy storage materials, E_b and polarization are usually a pair of contradictory properties. And most materials tend to have only one of them at the most [112]. How to resolve such paradox becomes the key to improve the energy storage performance.

1) E_b

In general, the energy density of capacitors is related to the square of E_b, and thus E_b is an important parameter affecting the energy storage performance [121–124]. Factors affecting E_b of ceramics include but are not limited to sample thickness, grain size, relative density, temperature, voltage type, and electrode shape/size [25]. According to the restrictive factors of E_b, breakdown mechanisms are classified as intrinsic breakdown, electromechanical breakdown, thermal breakdown, partial discharge breakdown, etc. [25,121,122]. This subsection mainly focuses on how to enhance the intrinsic breakdown, which is the most widely investigated.

The E_g refers to the forbidden energy between the top of the valence band (VB) and the bottom of the conduction band (CB), which is usually closely related to the intrinsic dielectric breakdown [60].

$$E_b = 1.36\times10^7 (E_g / 4.0)^3 (\mathrm{V/cm}) \quad (7)$$

In general, E_g > 4.0 eV is considered to be insulated, and 0.0 eV < E_g < 4.0 eV and E_g = 0.0 eV are regarded as semiconductors and metals, respectively. The E_g can be enhanced by forming the solid solution with enhanced resistivity, leading to the increment in E_b [125,126].

Figure 10(a) shows the E_g of various lead-free energy storage ceramics. The highest value of ~3.5 eV is found in NN ceramics [48,53,109,112,127–130]. Therefore, NN is often chosen as an additive to enhance the E_g of other dielectric ceramics. Qi *et al*. [24] studied the $(0.67-x)BiFeO_3$–$0.33BaTiO_3$–$xNaNbO_3$ (BF–BT–NN) ceramics, as shown in Fig. 10(b), where the E_g of BF-based ceramics monotonously increases with the NN content. The larger E_g means the more difficulty for electrons to jump from VB to CB, and thus larger E_b [60]. Finally, E_b is enhanced to 360 kV/cm at x = 0.1 (Fig. 10(c)). And W_{rec} and η achieve ~8.12 J/cm^3 and ~90%, respectively (Fig. 10(d)).

$CaHfO_3$ (CH) is a compound with ultra-large E_g of ~6.4 eV [61]. It is rational to utilize it as a modifier to optimize the E_g, E_b, and energy storage performance of dielectric ceramics [61]. In the $(1-x)Bi_{0.47}Na_{0.47}Ba_{0.06}TiO_3$–$xCaHfO_3$ (BNBT–CH) ceramics, the highest E_g of ~3.24 eV is obtained in 0.88BNBT–0.12CH ceramics (Fig. 11(a)) [62]. Meanwhile, the E_b is improved from 120 to 280 kV/cm (Fig. 11(b)), and W_{rec} and η are elevated to 4.2 J/cm^3 and 66.7%, respectively (Fig. 11(c)), which are 711% and 138% of the BNBT without CH, respectively. Similarly, after adding $Ca(Hf_{0.2}Ti_{0.8})O_3$ (CHT) to AN ceramics, E_g increases from 2.72 to 2.80 eV (Fig. 11(d)), and E_b enhances from 200 to 325 kV/cm (Fig. 11(e)). The best comprehensive performance is obtained in $0.94AgNbO_3$–$0.06Ca(Hf_{0.2}Ti_{0.8})O_3$ (AN–CHT0.06) ceramics with the W_{rec} of ~5.4 J/cm^3 and η of ~66% (Fig. 11(f)) [61]. Dai *et al*. [131] optimized the energy storage performance via increasing the E_g to ~3.21 eV and reducing the grain size to ~0.21 μm in 0.825 $(K_{0.5}Na_{0.5})NbO_3$–$0.175Sr(Sc_{0.5}Nb_{0.5})O_3$ (0.825KNN–0.175SSN) ceramics, leading to a high E_b of 395 kV/cm and W_{rec} of 4.42 J/cm^3.

2) Polarization

$Bi(Me'Me'')O_3$ (Me' = Mg^{2+} and Zn^{2+}; Me'' = Ti^{4+} and Nb^{5+}) are used to enhance the polarization of ceramics due to their unique configuration of lone pair electrons of Bi^{3+} 6s, which is capable of hybridization with O^{2-} 2p orbitals, leading to the high polarization of Bi-based ceramics [132–136]. At the same time, the introduction of $Bi(Me'Me'')O_3$ facilitates forming PNRs, which are easier to align and switch back with the loading and unloading external electric

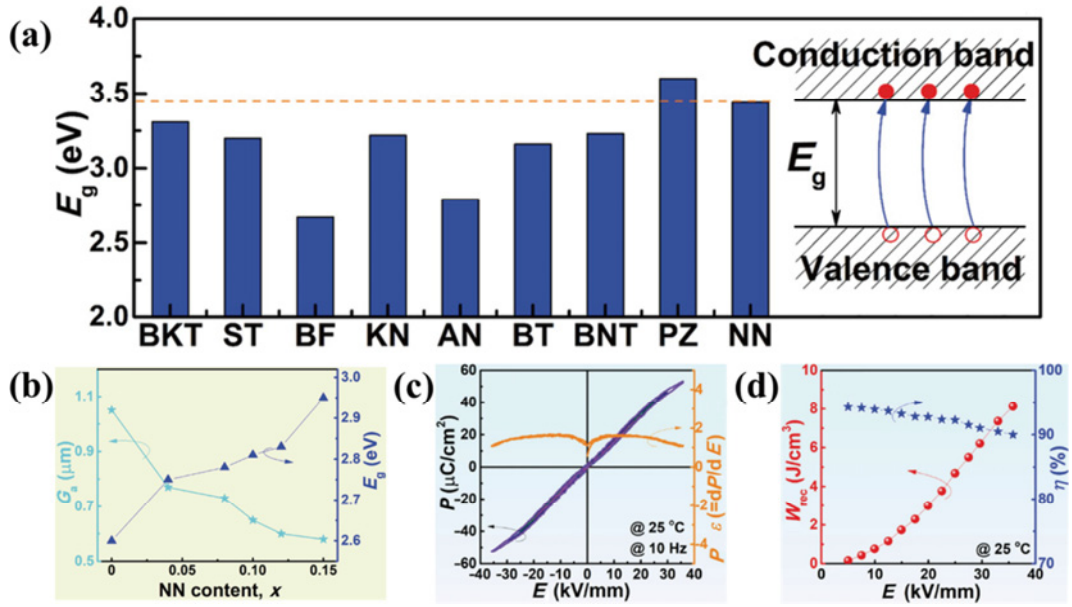

Fig. 10 (a) Comparison of E_g values between different ceramics. (b) Variation of grain size (G_a) and E_g of BF–BT–NN ceramics. (c) *P*–*E* loops and (d) energy storage performance of BF–BT–NN ceramics. Reproduced with permission from Ref. [116] for (a), © WILEY-VCH Verlag GmbH & Co. KGaA, Weinheim 2019; Ref. [24] for (b–d), © WILEY-VCH Verlag GmbH & Co. KGaA, Weinheim 2019.

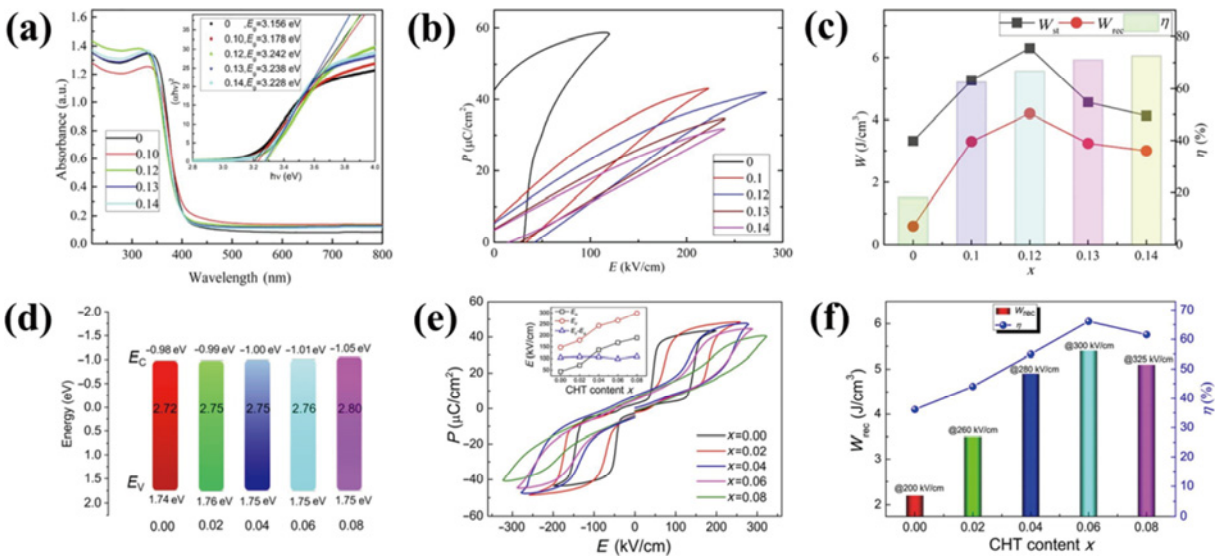

Fig. 11 (a) Ultraviolet–visible absorbance spectra and optical E_g of BNBT–CH ceramics. (b) *P*–*E* loops and (c) energy storage performance of BNBT–CH ceramics. (d) Schematic diagram of energy band structures of AN–CHT ceramics, where E_C and E_V are the energy of the CB and VB, respectively. (e) *P*–*E* loops and (f) energy storage performance of AN–CHT*x* ceramics. Reproduced with permission from Ref. [62] for (a–c), © Elsevier B.V. 2021; Ref. [61] for (d–f), © Elsevier B.V. 2021.

fields, and thus show small P_r in *P*–*E* loops [64]. In general, the P_{max} of dielectric ceramics generally decays with the increment of doping elements. However, the opposite phenomenon is observed in BT–$Bi(Mg_{1/2}Hf_{1/2})O_3$ (BT–BMH) ceramics [84]. As shown in Figs. 12(a)–12(c), the P_{max} of BT–BMH ceramics increased slightly after doping [84], which is attributed to the orbital hybridization of Bi^{3+} 6s with O^{2-} 2p and the increased E_b simultaneously. With the synergic effect of enhanced P_{max}, E_b, and suppressed P_r, the W_{rec} and η of BT-based ceramics go up to 3.38 J/cm^3 and 87% at 240 kV/cm, respectively (Fig. 12(d)). BMN is also introduced into $0.7Bi_{0.5}Na_{0.5}TiO_3$–$0.3Sr_{0.7}Bi_{0.2}TiO_3$ (BNT–SBT) ceramics to realize a small P_r of

~1.5 μC/cm^2 and high P_{max} of ~48 μC/cm^2. A large $P_{max} - P_r$ of ~46 μC/cm^2 is achieved in BNT–SBT–BMN ceramics (Fig. 12(e)), leading to ultra-high W_{rec} of 7.5 J/cm^3 and η of 92% (Fig. 12(f)) [47]. In addition to BMH and BMN, many other Bi-based perovskite compounds are also demonstrated to be effective to enhance polarization, such as $Bi(Ni_{2/3}Nb_{1/3})O_3$, $Bi(Mg_{0.5}Ti_{0.5})O_3$, and BMZ, as shown in Table 2.

W^{6+} is also commonly used to enhance the polarization. After introducing W^{6+} into AN ceramics, a significant decrement in P_r and an increment in P_{max} are observed, which favor the energy density a lot (Figs. 13(a) and 13(b)) [142]. The doping of W^{6+} alleviates the oxygen vacancies, weakens the pinning effect, and thus enhances the polarization [30]. In addition, W^{6+} can also stabilize the antiferroelectricity and increase the critical phase transition electric fields. W_{rec} of 3.3 J/cm^3 and η of 50% are finally obtained at 200 kV/cm (Fig. 13(c)). W^{6+} can also improve the ferroelectricity in PZO film [143]. W^{6+} replacement of Zr^{4+} gives rise to lattice distortion and ferroelectricity in PZO film, thus leading to higher polarization (Fig. 13(d)).

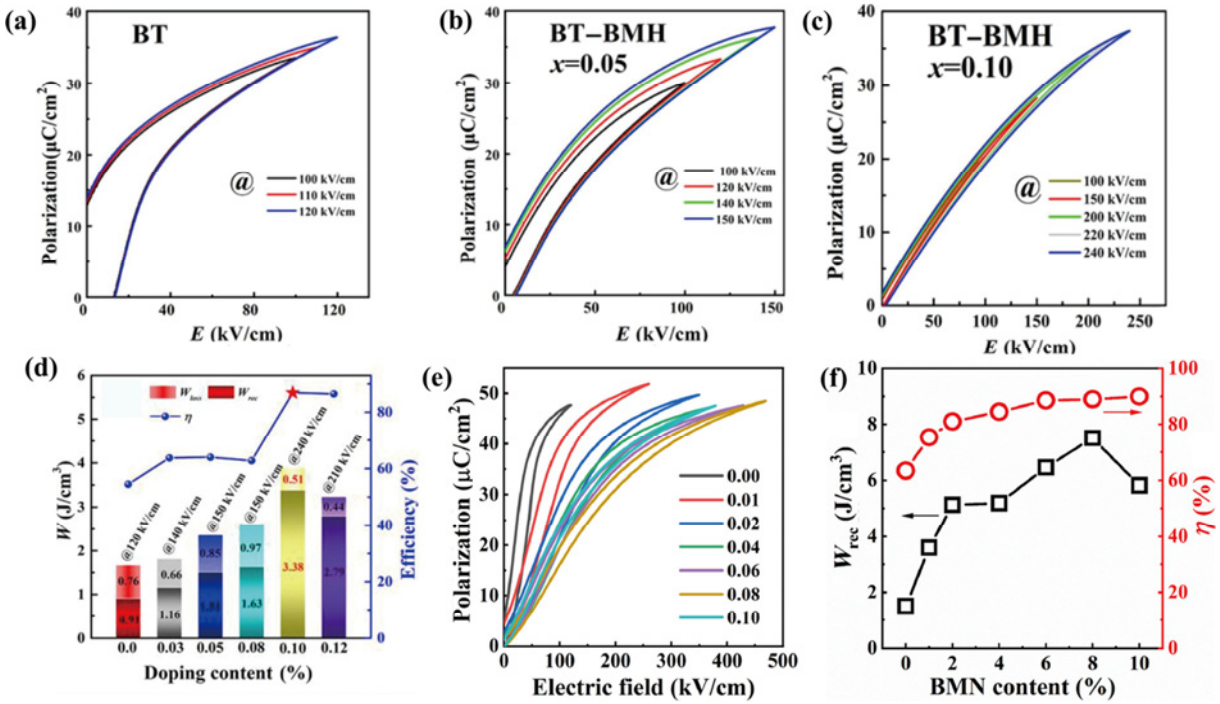

Fig. 12 (a–c) *P*–*E* loops and (d) energy storage performance of BT–BMH ceramics. (e) *P*–*E* loops and (f) energy storage performance of BNT–SBT–BMN ceramics. Reproduced with permission from Ref. [84] for (a–d), © Elsevier B.V. 2021; Ref. [47] for (e, f), © Elsevier B.V. 2021.

Table 2 Energy storage performance of ceramics containing $Bi(Me'Me'')O_3$

Composition	P_{max} (μC/cm^2)	W_{rec} (J/cm^3)	η (%)	E_b (kV/cm)	Ref.
$0.88BT–0.12Bi(Ni_{2/3}Nb_{1/3})O_3$	24.01	2.09	95.9	200	[137]
$0.88BT–0.048Bi(Li_{0.5}Nb_{0.5})O_3–0.072Bi(Mg_{0.5}Ti_{0.5})O_3$	22.5	2.4	91.5	290	[138]
$0.85BT–0.15Bi(Mg_{0.5}Zr_{0.5})O_3$	23.2	2.9	86.8	300	[32]
$0.9BST–0.1Bi(Mg_{2/3}Nb_{1/3})O_3$	21.5	3.34	85.71	400	[139]
$0.925BCZT–0.075Bi(Mg_{2/3}Nb_{1/3})O_3$	26.2	3.81	90.5	405	[64]
$0.6BT–0.4Bi(Mg_{1/2}Ti_{1/2})O_3$	42.2	4.49	93	340	[140]
$0.62NBT–0.3SBT–0.08Bi(Mg_{2/3}Nb_{1/3})O_3$	48	7.5	92	470	[47]
$0.97AN–0.01Bi(Zn_{2/3}Nb_{1/3})O_3$	53.8	4.6	57.5	220	[119]
$0.35BF–0.65(0.85BT–0.15Bi(Sn_{0.5}Zn_{0.5})O_3)$	38.5	3.06	92	185	[141]

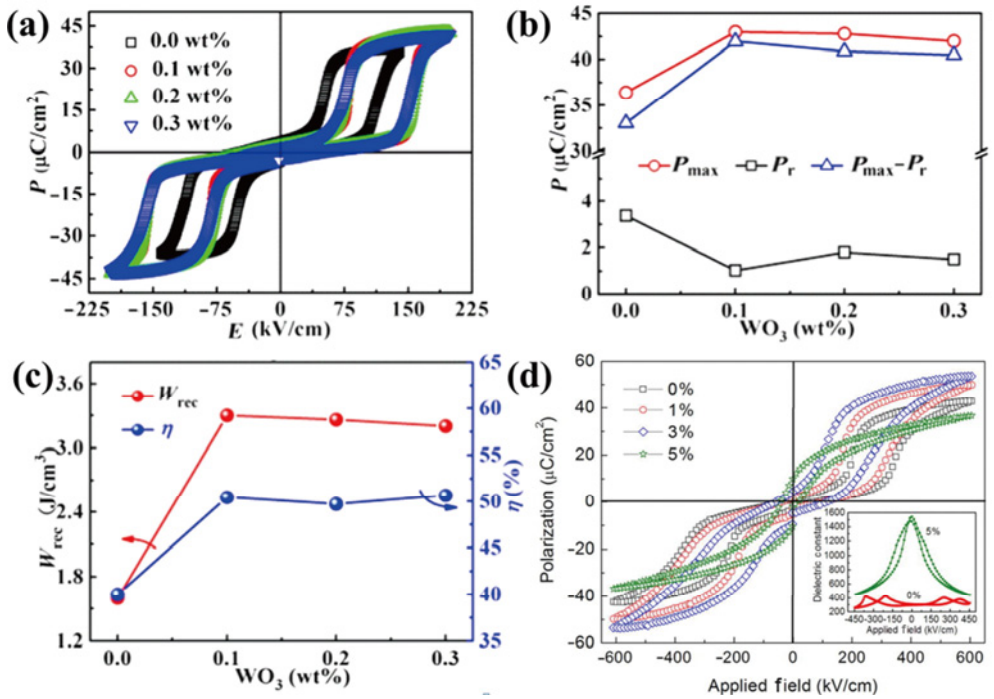

Fig. 13 (a) *P*–*E* loops, (b) $P_{max} - P_r$, and (c) energy storage performance of W^{6+}-doped AN ceramics. (d) *P*–*E* loops of W^{6+}-doped PZO films. Reproduced with permission from Ref. [142] for (a–c), © American Chemical Society 2017; Ref. [143] for (d), © AIP Publishing LLC 2013.

Besides, there are other methods to enhance the polarization. For example, Nd^{3+}-doped AN induces $Nd_{Ag}^{\cdot\cdot}$ and V'_{Ag} at A-sites [31]. The polarization increases from ~43 to ~60 μC/cm^2, which may be related to the increased concentration of silver vacancies [30]. Wang *et al*. [144] utilized an average ionic polarizability design strategy to enhance the W_{rec} by sustaining high polarization and simultaneously improved η by disrupting the polar order in $(1-x)$(0.7BNT–0.3SBT)–xSr$(Zn_{1/3}(Nb_{0.85}Ta_{0.15})_{2/3})O_3$ ceramics. The polarization was finally stabilized at > 41 μC/cm^2, and the W_{rec} and η were as high as 5.2 J/cm^3 and 91%, respectively.

In some cases, the introduction of doping elements can not only enhance the polarization but also reduce the ceramic grain size, leading to high P_{max} and E_b [27,30]. For example, Gao *et al*. [145] introduced $Bi(Mg_{0.5}Sn_{0.5})O_3$ (BMS) into $(Na_{0.5}Bi_{0.5})_{0.65}Sr_{0.35}TiO_3$ (NBST) ceramics. When the BMS content raises from 0 to 10 mol%, the ceramic grain size reduces from 4.17 to 0.67 μm, and the E_b enhances from 220 to 405 kV/cm. Moreover, due to the strong orbital hybridization of Bi^{3+} 6s with O^{2-} 2p, the P_{max} of NBST–BMS increases from ~46 to ~51 μC/cm^2. Finally, the W_{rec} of 6.68 J/cm^3 and η of 89.1% are obtained [132,141]. Zhang *et al*. [146] prepared KNN-based ceramics with high P_{max} of ~48 μC/cm^2 and high E_b of ~330 kV/cm via introducing $(K_{0.7}Bi_{0.3})NbO_3$. The P_{max} and E_b are enhanced by 33% and 230%, respectively, over the undoped samples.

3. 2 Microscale modification

3.2.1 Core–shell structure

It is reported that the shell, which is only a few nanometers thick near the grain boundaries, displays different compositions and properties from the core part [66]. The core–shell structure in ceramics is generally composed of FE, RFE, or non-FE (such as LD material and glass) [21]. For example, adding glass powders to FE ceramics is a common method to fill at the grain boundaries and enhance the E_b [147,148]. Similarly, combining the glass phase with $(Pb_{0.97}La_{0.02})(Zr_{0.56}Sn_{0.35}Ti_{0.09})O_3$ ceramics can change the E_b from 110 to 150 kV/cm, while the energy density is increased to 3.3 J/cm^3 [101]. Wu *et al*. [149] constructed an "FE–paraelectric" core–shell structure via wrapping BT grains with ST, which simultaneously enhances the E_b and maintains high dielectric constants.

Recently, Yuan *et al*. [28] reported a unique bioinspired raspberry-like hierarchically structure of $x$wt%BT–BMZ/$BaTiO_3$–$Bi(Mg_{0.5}Zr_{0.5})O_3$@SiO_2 (BBSx)

nanograins, as shown in Fig. 14(a). The experimental characterization and theoretical simulation confirm that the synergic effect of raspberry-like structure and insulating SiO_2 nanocoating significantly improves the E_b and sustains large polarization of the nanocomposites [28,150]. $BaTiO_3$–$Bi(Mg_{0.5}Zr_{0.5})O_3$@SiO_2 (BT–BMZ@SiO_2) fine powders with a grain size of ~50 nm are obtained via the high-energy ball milling and SiO_2 coating, followed by the mixing with BT–BMZ of ~500 nm to gain composites (Fig. 14(b)). The phase field simulations (Fig. 14(c)) reveal that the ceramics with 7 wt% nano-fine powders exhibit the most complex breakdown path. Together with a large polarization guaranteed by the submicron BT–BMZ grains, BBS7 ceramics display a W_{rec} of 3.14 cm^3 with η of 85.1%.

Jin *et al*. [66] prepared a kind of $BaTiO_3$@$(K,Na)NbO_3$ (BT@KNN) ceramics, and the KNN shell was fabricated on BT grains of ~50 nm. Many nanodomain structures with sizes less than 100 nm can be observed, which is sensitive to the electric field response with low potential barriers. Moreover, the coexistence of the R-phase and the T-phase can be observed at the core position. Multiple nanodomain structures in BT@KNN ceramics are beneficial to low hysteresis and P_r, while the BT phase can maintain large P_{max}. Therefore, a large $P_{max} - P_r$ of ~21.3 μC/cm^2 is obtained at 210 kV/cm, leading to W_{rec} of ~1.91 J/cm^3 and η of ~84.8%.

Core–shell structures can combine two materials with different properties to break the paradox between some parameters, such as polarization and E_b. By wrapping a layer of SiO_2 on the surface of AN, E_b is raised from 180 to 250 kV/cm, while P_{max} is stabilized at 34.5 μC/cm^2 [21]. Based on this, Bi^{3+} and Sc^{3+} are introduced, and E_b is further increased to 322 kV/cm, while P_{max} is increased to 45 μC/cm^2 [27]. Wang *et al*. [151] prepared $BaTiO_3$@3% FeO (BT@FeO) ceramics with grain sizes of ~70 nm by coating the FeO layer on the surface of BT particles via the sol–gel method. The energy density and energy efficiency are 1.5 J/cm^3 and 88%, respectively, which are 500% and 175% higher compared to those of the uncoated one, respectively. Table 3 summarizes the energy storage performance of ceramics with core–shell structures.

3.2.2 0–3 type composite

According to the reported organic–inorganic composites, interfacial effects can significantly enhance the energy storage performance [8,158]. Similarly, the energy storage performance can also be optimized by designing 0–3 type composites in inorganic materials [69,70,72].

Recently, Li *et al*. [69] reported a novel 0–3 type $(Bi_{0.32}Sr_{0.42}Na_{0.20})TiO_3$/MgO (BNST/MgO) composite with high E_b, as shown in Fig. 15(a). Compared with $(Bi_{0.32}Sr_{0.42}Na_{0.20})TiO_3$ ceramics with high ε_r of ~1900, the ε_r of MgO and $MgTiO_3$ are as low as 10 and 17, respectively (Fig. 15(b)). The results of the phase field simulations show that there existed a distortion of the electric potential and local electric field after the MgO/$MgTiO_3$ second phase with low ε_r is introduced

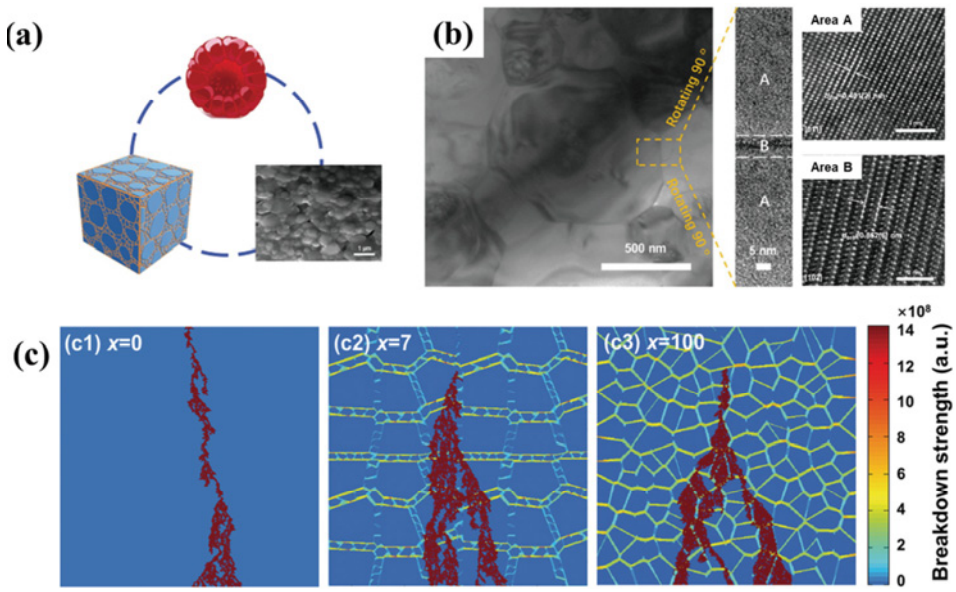

Fig. 14 (a) Raspberry-like hierarchically structures of BBS*x* ceramics. (b) Representative bright-field TEM image of the BBS7 ceramics. (c) Breakdown paths of BBS*x* ceramics (x = 0, 7, and 100) simulated by the finite element method. Reproduced with permission from Ref. [28], © WILEY-VCH Verlag GmbH & Co. KGaA, Weinheim 2020.

Table 3 Energy storage performance of ceramics with core–shell structures

Composition	Grain size (μm)	E_b (kV/cm)	W_{rec} (J/cm^3)	η (%)	Ref.
BT–BMZ/BT–BMZ@SiO_2	0.2	345	3.41	85.1	[28]
BT@NiO	1	230	2.72	70	[152]
BT@FeO	0.07	300	1.5	88	[151]
BT@KNN	0.194	211	2.24	84.8	[66]
BT@2 wt% SiO_2	—	202	1.2	53.8	[71]
0.95(BT–BNT–Nb)–0.05BNT	—	230	1.91	91	[153]
Mn–AN@SiO_2	2.72	244	3.34	60	[21]
Mn–AN@SiO_2+Bi/Sc	2.2	322	5.9	71	[27]
(BNT@La_2O_3)–($SrSn_{0.2}Ti_{0.8}O_3$@La_2O_3)–Bi_2O_3–B_2O_3–SiO_2	0.76	275	2.25	82.1	[154]
0.96(0.65BNT–0.35$Sr_{0.85}Bi_{0.1}TiO_3$)–0.04NN	1.48	248	3.08	81.4	[155]
$Pb_{0.91}La_{0.06}(Zr_{0.552}Sn_{0.368}Ti_{0.08})O_3$@PbO–$B_2O_3$–$SiO_2$–$Al_2O_3$–ZnO–$MnO_2$	1.5	402	7.4	55.3	[156]
$Pb_{0.97}La_{0.02}(Zr_{0.33}Sn_{0.55}Ti_{0.12})O_3$@$SiO_2$	—	238	2.68	—	[157]

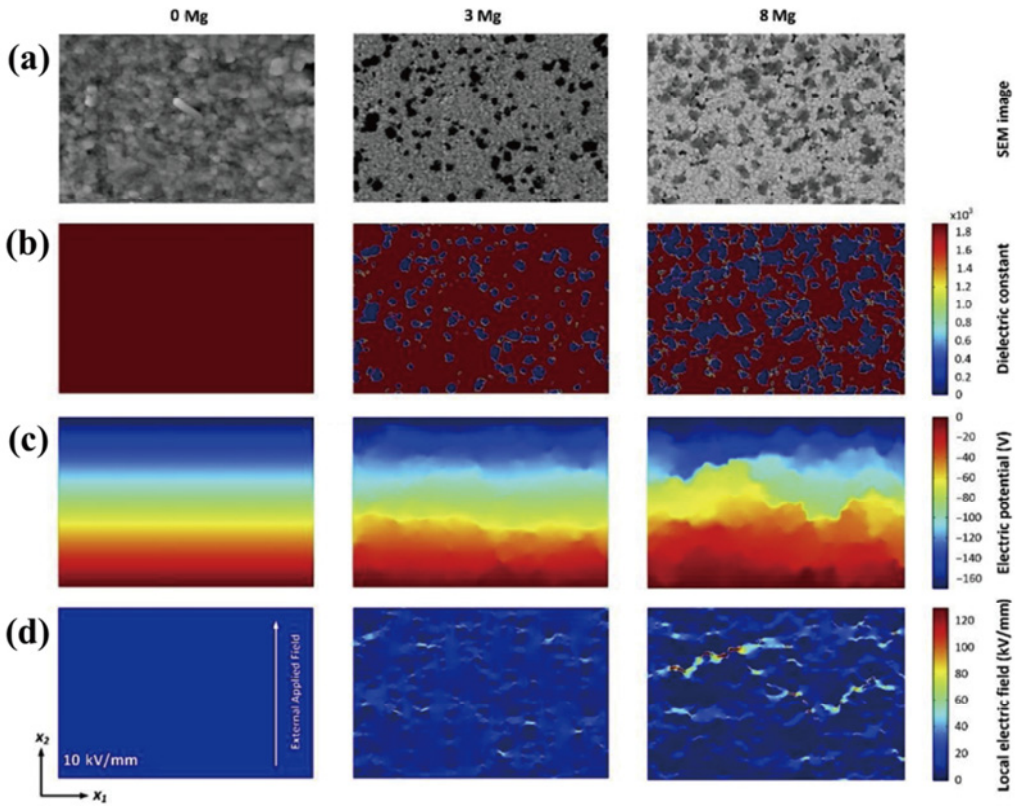

Fig. 15 (a) SEM images of BNST/MgO ceramics. (b) Dielectric constants, (c) electric potentials, and (d) local electric fields of BNST/MgO ceramics. Reproduced with permission from Ref. [69], © Elsevier Ltd. 2019.

into the BNST ceramics, and more equipotential lines concentrate to a lower value (Figs. 15(c) and 15(d)). Thus the E_b of the BNST/MgO ceramics changes from 120 to 200 kV/cm via adding 3 wt% MgO insulation phase, and the W_{rec} of 2.09 J/cm^3 with η of 84% is obtained. Tao *et al*. [70] increased the E_b of 0.82(0.94BNT–0.06BT)–0.18KNN ceramics from 90 to 140 kV/cm via introducing the ZnO second phase. At the ZnO content of 0.4 wt%, the W_{rec} of 1.03 J/cm^3 and η of 72.7% are obtained.

3.3 Mesoscale modification

The effect of grain size on the energy storage performance is achieved by affecting E_b [40,150,159].

$$E_b \propto (\text{Grain size})^{-a} \quad (8)$$

where a is in the range of 0.2–0.4 [25,150,160]. In general, the smaller the grain size, the higher the E_b is [25,150,160–162]. This is mainly due to the formation of the depletion space charge layers at the grain boundary, which efficiently increases the boundary resistivity [25]. As a result, the leakage current decreases in fine-grain ceramics, beneficial to a large E_b [25]. Up to now, many methods have been successfully utilized in ceramics to reduce grain sizes, such as high-energy ball milling [29,73], novel sintering method [74,163–165], and hydrothermal synthesis [21,22,27,75].

3.3.1 *High-energy ball milling*

High-energy ball milling is very powerful to reduce the powder size of raw materials through the rotation or vibration, so that the reaction activation energy is dramatically reduced, and the sintering activity is enhanced [166].

Recently, Chen *et al*. [29] successfully reduced the grain size to ~178 nm (Fig. 16(a)) via high-energy ball milling in $0.6Bi_{0.5}K_{0.5}TiO_3$–$0.3BaTiO_3$–$0.1NaNbO_3$ (0.6BKT–0.3BT–0.1NN) ceramics (Fig. 16(b)). Nanoscale grain sizes, dense grain boundaries, ultra-small PNRs, and large E_g give rise to an ultra-high E_b of 460 kV/cm and excellent W_{rec} of ~7.57 J/cm^3, which is 2.4 times higher than that of previously reported BKT ceramics (Fig. 16(c)) [29]. Moreover, it can be seen that nanoscale modifications and mesoscale modifications are not incompatible. By contrast, they can work together to synergistically improve the energy storage performance.

Compared to that of $BiFeO_3$–$BaTiO_3$–$Bi(Mg_{2/3}Nb_{1/3})O_3$ (BF–BT–BMN) ceramics prepared via the conventional solid-state (CS) reaction, the grain size prepared via high-energy ball milling reduces from 4.1 to 0.89 μm (Figs. 17(a) and 17(b), respectively) [73]. The TEM reveals layered domains with a width of 80–100 nm in coarse-grained ceramics, while PNRs with a width of ~2 nm are observed in fine-grained ceramics [167]. Therefore, the fine-grained BF–BT–BMN ceramics respond quickly to the external electric field, facilitating the slim and slanted P–E loops (Fig. 17(c)). Most importantly, the E_b increases from 50 to 110 kV/cm due to the decreased in grain size. Finally, the W_{rec} of fine-grain ceramics (1.27 J/cm^3) reaches about 8 times higher than that of coarse-grain ceramics (0.16 J/cm^3), as shown in Fig. 17(d).

3.3.2 *Novel sintering method*

Two-step sintering is an effective method to obtain fine-grain ceramics by adjusting the sintering temperature and time. In the one-step sintering process, grain boundary migration and diffusion are always active during both the heating and preservation stage, leading to the grain growth and uneven distribution [74]. During the two-step sintering process, the ceramics are heated to a higher temperature (T_1) in the first stage to promote the grain migration and diffusion. In the second stage, the ceramics are rapidly cooled to a lower temperature (T_2) and kept for some time. Grain boundary migration and diffusion are thus inhibited, and the grains reach a full density with limited grain boundary diffusion (Fig. 18) [163,168,169].

The $0.89Bi_{0.5}Na_{0.5}TiO_3$–$0.06BaTiO_3$–$0.05K_{0.5}Na_{0.5}NbO_3$ (BNT–BT–KNN) ceramics prepared via one-step sintering have uneven grain distribution and anomalous grains (Fig. 19(a)), while the ceramics with two-step sintering exhibit a much denser crystal morphology with smaller and more homogeneous grains (Fig. 19(b)), leading to the much increased E_b (Fig. 19(c)) [40,150].

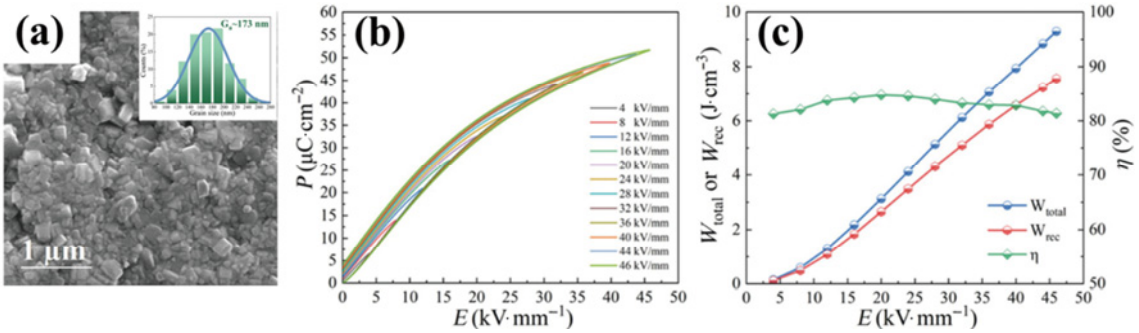

Fig. 16 (a) SEM image of 0.6BKT–0.3BT–0.1NN ceramics. (b) P–E loops and (c) energy storage performance of 0.6BKT–0.3BT–0.1NN ceramics. Reproduced with permission from Ref. [29], © Wiley-VCH GmbH 2021.

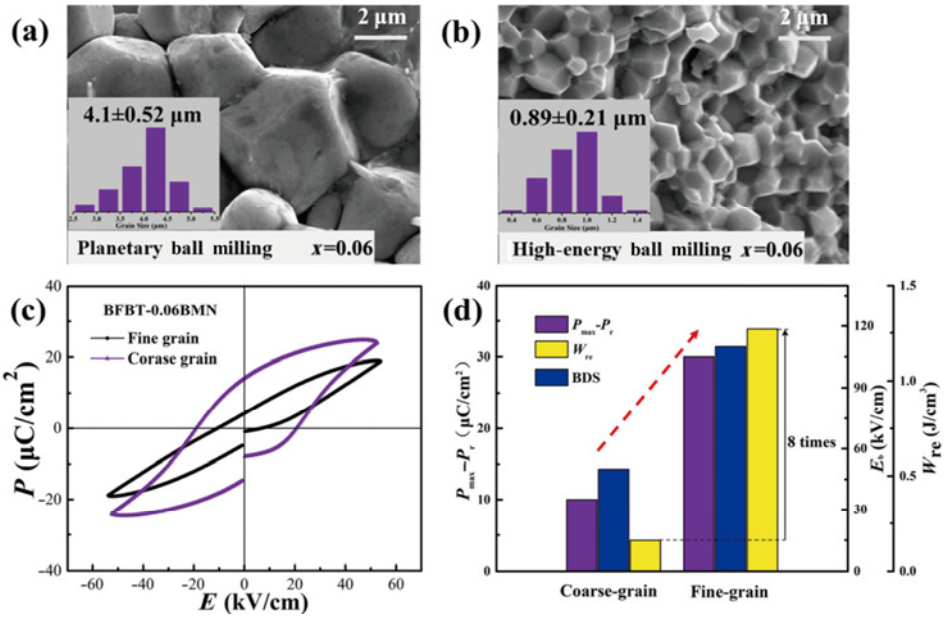

Fig. 17 SEM images of BF–BT–0.06BMN ceramics prepared via (a) planetary ball milling and (b) high-energy ball milling. (c) *P*–*E* loops and (d) energy storage performance of BF–BT–0.06BMN ceramics. Reproduced with permission from Ref. [73], © Elsevier Ltd and Techna Group S.r.l. 2021.

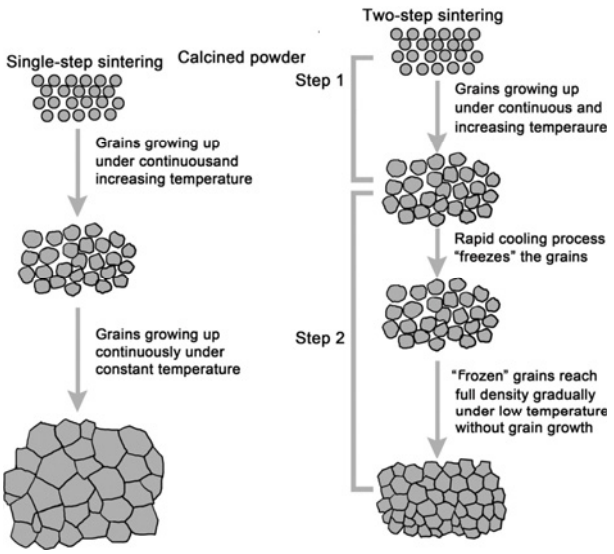

Fig. 18 Different mechanisms of grain growth in one-step sintering process and two-step sintering process. Reproduced with permission from Ref. [74], © Elsevier B.V. 2013.

Wang *et al*. [164] combined high-energy ball milling with a two-step sintering process and successfully reduced the grain size of $0.925(K_{0.5}Na_{0.5})NbO_3$–$0.075Bi(Zn_{2/3}(Ta_{0.5}Nb_{0.5})_{1/3})O_3$ (KNN–BZTN) ceramics from 410 to 200 nm (Figs. 20(a) and 20(c), respectively). Accordingly, E_b is increased from 208 to 301 kV/cm. They found that the higher temperature and shorter holding time for the second stage give rise to the smaller grain size and denser microstructures [164]. With a higher temperature, more liquid phase is generated in the ceramics (indicated by the yellow regions in Fig. 20(a1)), while the shorter holding time makes it insufficient for the diffusion, which results in the smaller grain size and more amorphous grain boundaries (Figs. 20(b) and 20(d), respectively) [164]. As a result, the larger resistivity is observed and E_b is increased, doing a great favor to the optimized W_{rec} of 4.02 J/cm^3 and η of 87.4%.

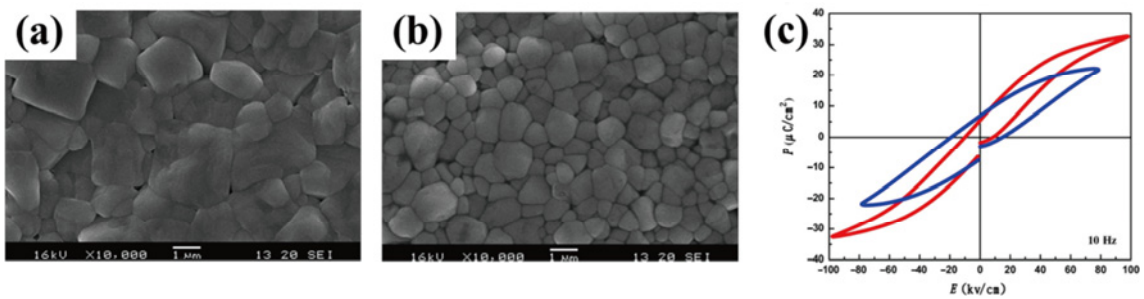

Fig. 19 SEM images of BNT–BT–KNN ceramics sintered via (a) one-step sintering and (b) two-step sintering. (c) *P*–*E* loops of different sintering methods. Reproduced with permission from Ref. [74], © Elsevier B.V. 2013.

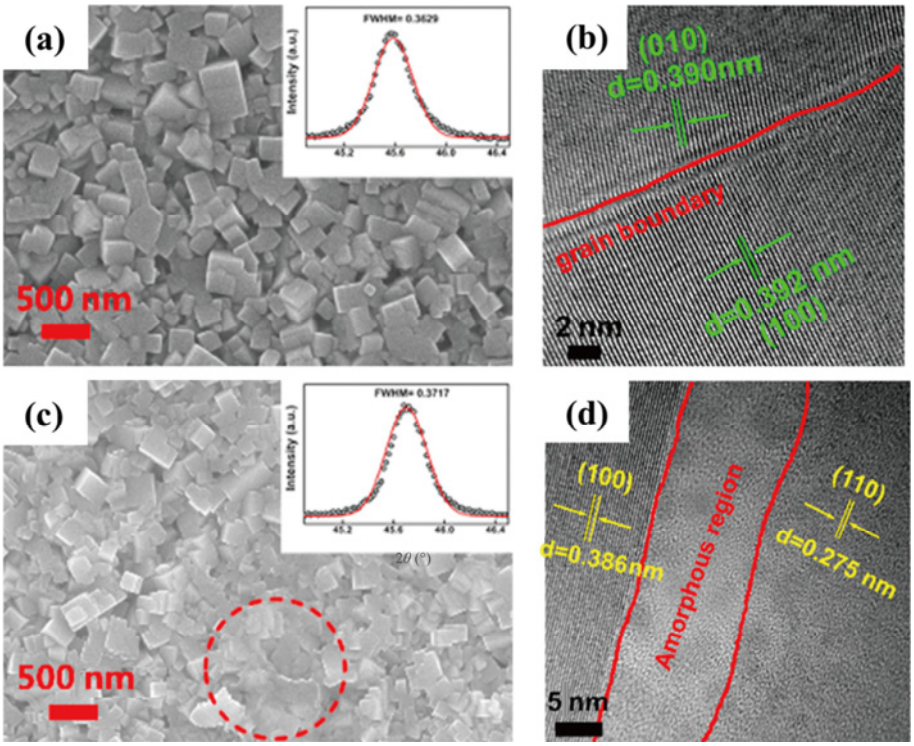

Fig. 20 SEM and high-resolution TEM (HRTEM) images of KNN–BZTN ceramics with different temperature and time: (a, b) 1130 ℃, 15 h and (c, d) 1160 ℃, 6 h. Note: FWHM means the full width at half maximum. Reproduced with permission from Ref. [164], © The Chinese Ceramic Society 2020.

The two-step sintering is also widely used in other systems. $0.83NaNbO_3$–$0.17SrTiO_3$ (NN–ST) ceramics prepared via the two-step process show the grain size of ~1.2 μm and E_b of 207 kV/cm [170]. With the decrement in heating/holding temperature and holding time, the grain size gradually decreases from 8.2 to 1.2 μm, which is conducive to the improvement of E_b (from 128 to 207 kV/cm). Meanwhile, the W_{rec} and η increase from 0.58 J/cm^3 and 42% to 1.60 J/cm^3 and 50%, respectively. Compared with that of the solid-state sintering, the grain size of $BiFeO_3$–$SrTiO_3$ (BF–ST) ceramics prepared via two-step sintering was only 3.2 μm, showing a remarkable decrease by 36% over counterparts prepared by the solid-state sintering [171]. Meanwhile, the E_b increased from 626 to 750 kV/cm, and the ultra-high W_{rec} of 8.4 J/cm^3 with η of ~90% was obtained. With the help of two-step sintering, the minimal ceramic grains of ~326 nm was achieved in $0.13Bi(Zn_{2/3}(Nb_{0.85}Ta_{0.15})_{1/3})O_3$ (BZNT)@0.6 wt%SiO_2 MLCC [58]. As a result, the large E_b of 1755 kV/cm was achieved and contributed to the great improvement of W_{rec} and η by 1261% and 1.9%, respectively.

Besides the two-step sintering, there are some other sintering processes that can also be employed to improve the energy storage performance. For example, spark plasma sintering (SPS) displays the characteristics of low sintering temperature, rapid heating rate, and short sintering time [172–174]. SPS could effectively suppress the diffusion behavior between the tetragonal $(Pb_{0.858}Ba_{0.1}La_{0.02}Y_{0.008})(Zr_{0.65}Sn_{0.3}Ti_{0.05})O_3$ (PBLYZST) and the orthorhombic $(Pb_{0.97}La_{0.02})(Zr_{0.9}Sn_{0.05}Ti_{0.05})O_3$ (PLZST), thus enhancing the FE–AFE switching electric field of PBLYZST–PLZST ceramics to 162 kV/cm. Finally, the W_{rec} is enhanced to 6.40 J/cm^3, which is higher than that of CS sintering sample. In addition, hot-press (HP) sintering exposes pressure during the sintering process to promote contact diffusion between particles, which can effectively eliminate pores and refine the grain size [175,176]. $Bi_{0.5}K_{0.5}TiO_3$–$Ba(Mg_{1/3}Nb_{2/3})O_3$ (BKT–BMN) ceramics prepared via the HP process achieve a W_{rec} of 3.14 J/cm^3, which is more than two times than that of the sample prepared by the CS sintering [177].

3.3.3 *Hydrothermal synthesis*

Hydrothermal synthesis is regarded as one of the most suitable methods to obtain fine powders, which is conducive to the preparation of fine-grain ceramics [178,179]. Grain size reduction is an effective and widely used way to improve the E_b of ceramics without changing the chemical composition, as shown in Table 4.

Table 4 Energy storage performance of fine-grain ceramics

Composition	Preparation method	Grain size (μm)	E_b (kV/cm)	W_{rec} (J/cm^3)	η (%)	Ref.
AN	Hydrothermal	1.08	273	3.34	54.5	[75]
AN	Hydrothermal	3	216	3.26	53.5	[180]
AN	Hydrothermal	3.4	250	1.85	40	[22]
$Ag_{0.97}Nd_{0.01}NbO_3$+MnO_2	Two-step sintering	1.4	210	3.2	52	[181]
KNN–BZTN	Two-step sintering	0.2	222	4.02	87.4	[164]
NN–ST	Two-step sintering	1.20	207	1.60	50	[170]
$Sr_{0.7}Ba_{0.3}Nb_2O_6$	Two-step sintering	1.34	400	3.2	90	[182]
0.55(0.94BNT–0.06BT)–0.45ST+MnO_2	Two-step sintering	2.4	280	2.98	73.1	[183]
KNN-H	High-energy ball milling	0.6	740	10.6	90.8	[113]
0.6BKT–0.3BT–0.1NN	High-energy ball milling	0.18	460	7.57	81.4	[116]
$0.9Ba_{0.9}Ca_{0.1}Ti_{0.9}Zr_{0.1}O_3$–$0.1SrNb_2O_6$	High-energy ball milling	0.16	460	2.68	83.4	[184]

Wang *et al*. [22] successfully prepared AN fine powders with the particle size of ~480 nm via adjusting the ratio of NH_4HF_2, $AgNO_3$, and Nb_2O_5, from which AN ceramics with a grain size of ~3.4 μm were successfully prepared (Fig. 21(a)). Due to the small grain size, the E_b of AN is as large as 250 kV/cm

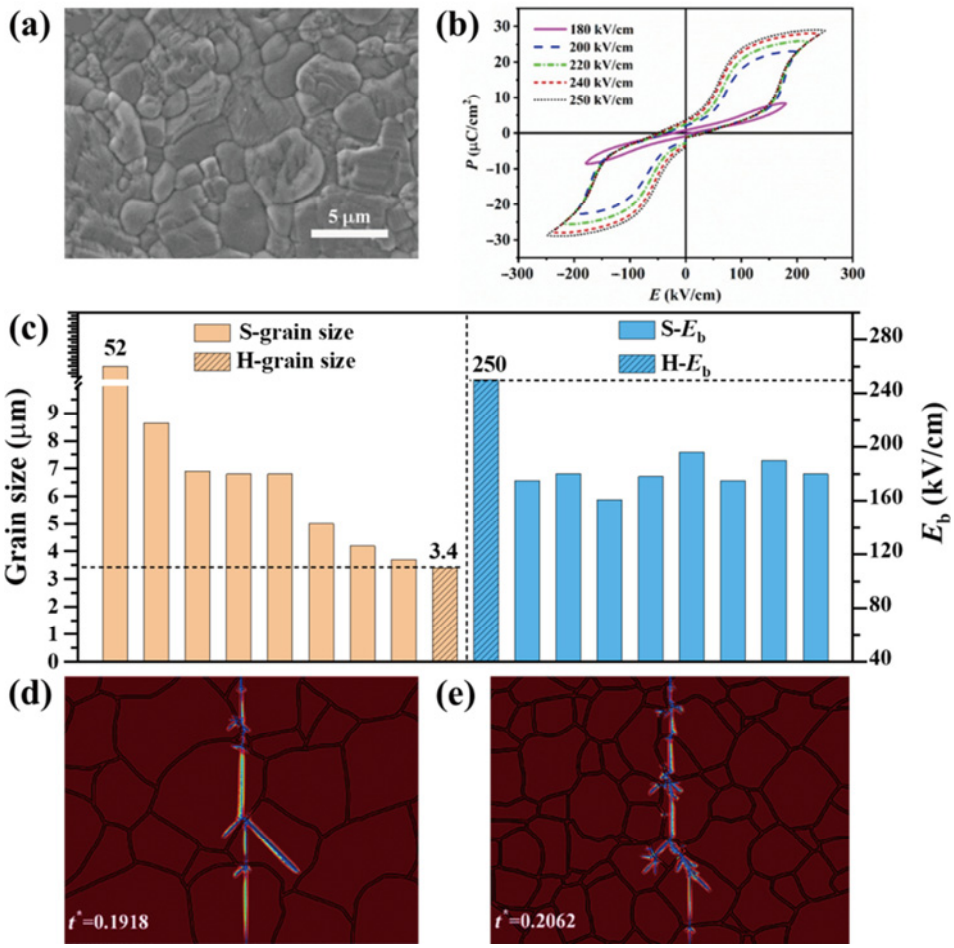

Fig. 21 (a) SEM images and (b) *P*–*E* loops of AN ceramics prepared via hydrothermal method. (c) Grain sizes and E_b of AN ceramics prepared by solid-state reaction and hydrothermal method. Breakdown simulations of AN ceramics prepared by (d) solid-state reaction and (e) hydrothermal method. Reproduced with permission from Ref. [22] for (a, b), © Elsevier Ltd. 2020; Ref. [75] for (d, e), © The Royal Society of Chemistry 2022.

(Fig. 21(b)). The AN ceramics exhibit smaller grain size and larger E_b compared to pure AN ceramics prepared by solid-state reaction (Fig. 21(c)) [34,65, 103,107–109,119,185]. A phase field model, which is used to simulate the spatial distribution of electric potential and electric breakdown paths, also indicates that the smaller grain size of AN ceramics prepared via the hydrothermal method (Figs. 21(d) and 21(e)) and the more breakdown-resistant grain boundaries lead to more energy consumption in the propagation of electrical trees [21,28,75,180]. Huang *et al*. [75] reported the synthesis of AN ceramics with a grain size of ~1.08 μm using the hydrothermal synthesized powders. The fine-grain size leads to the increment in E_b up to 273 kV/cm. Finally, the W_{rec} of 3.34 J/cm^3 and η of 54.5% are achieved in ceramics, which are 1.67 and 1.63 times larger than those prepared via the solid-state reaction, respectively.

3. 4 Macroscale modification

3.4.1 Rolling process

High porosity and poor densification of ceramics prepared via the CS reaction are two of the main reasons for the low E_b [76]. It is simple and effective to prepare energy storage ceramics with high densification and large E_b via the rolling process. As shown in Fig. 22(a), it involves mixing the ceramic powders with PVA and repeatedly squeezing it through two rotating rolls [48]. In this process, the pores are eliminated by pressure, and the PVA is fully contacted with the powders, giving rise to high-density ceramics [77]. Compared with other preparation processes, the rolling process is characterized by low-cost and simple equipment, which is widely used in the preparation of various ceramics [77,78].

In 2019, Wang *et al*. [48] prepared $(Pb_{0.98}La_{0.02})(Zr_{0.55}Sn_{0.45})_{0.995}O_3$ (PLZS) ceramics with high relative densities and E_b via the rolling process. The ceramics display smaller grain sizes, fewer pores, and higher relative densities (> 97%), which are expected to improve the E_b (Figs. 22(b) and 22(c)). Ultimately, the prepared PLZS ceramics exhibit an ultra-high W_{rec} of 10.4 J/cm^3 with η of 87% at 410 kV/cm, which is the highest W_{rec} value among the bulk materials at that time.

The rolling process is also applied to BT-based ceramics [186]. Compared with the CS reaction, the rolling process can reduce the grain size of $(Ba_{0.65}Sr_{0.245}Bi_{0.07})_{0.99}Nd_{0.01}TiO_3$ (BT–SBT–Nd) ceramics and make a uniform grain distribution [77]. The E_b of the ceramics increases from 275.5 to 468.9 kV/cm due to the improved relative densities, and the *P*–*E* curves exhibit a larger polarization of ~35 μC/cm^2. Finally, the W_{rec} of 4.2 J/cm^3 is obtained, which is ~2.1 times larger than that obtained via the CS reaction.

3.4.2 Tape-casting process

The tape-casting process involves mixing ceramic powders with solvents, dispersants, binders, and plasticizers to form a homogeneous suspension, which is then prepared into a thin, continuous ceramic ribbon using a scraper [187]. The ribbon has high relative densities and can be thinned to less than 50 μm in thickness [23,187]. Many layers of ceramic ribbons with electrodes coated via screen printing are stacked in a certain way and hot pressed. Finally, the MLCCs are obtained after burning out the binder by sintering, as shown in Fig. 23 [187]. The tape-casting process displays the following two advantages: (1) Compared to CS reaction, it facilitates ceramic layers with lower porosity and finer grain size, which lead to higher E_b [5]. (2) For the same capacitor volume, a higher E_b is expected in the MLCCs compared to that of the bulk ceramics, as the E_b exponentially increases with the decreased layer thickness [25,188].

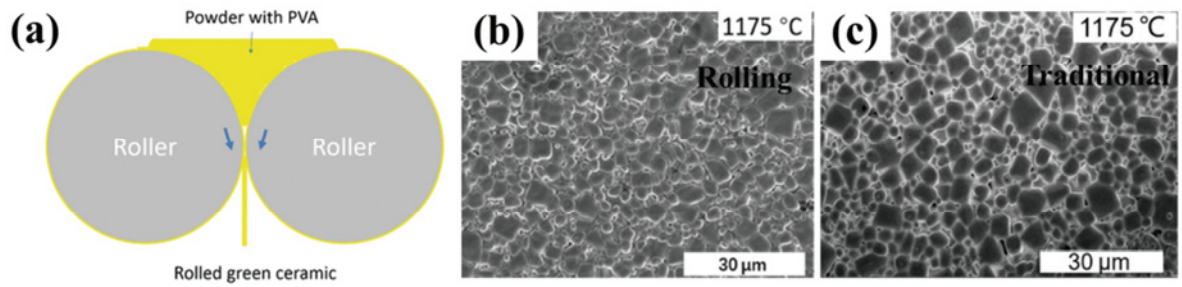

Fig. 22 (a) Schematic diagram of rolling process. SEM images of ceramics prepared via (b) rolling and (c) traditional method. Reproduced with permission from Ref. [48], © WILEY-VCH Verlag GmbH & Co. KGaA, Weinheim 2019.

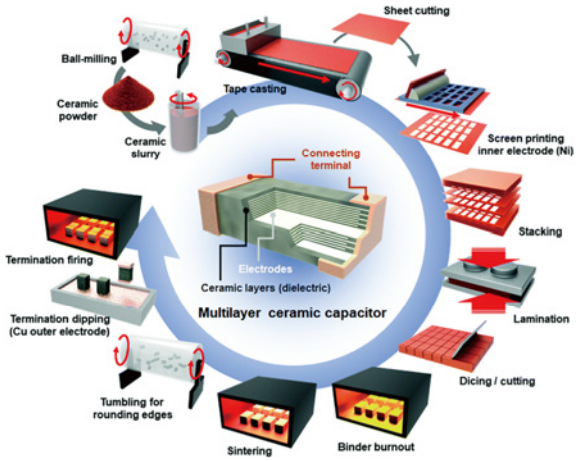

Fig. 23 Schematic diagram of MLCC preparation process. Reproduced with permission from Ref. [187], © IEEE 2010.

In 2018, Li *et al*. [5] prepared the $0.55(Na_{0.5}Bi_{0.5})TiO_3$–$0.45(Sr_{0.7}Bi_{0.2})TiO_3$ (0.55NBT–0.45SBT) MLCCs with an ultra-high energy density and energy efficiency via the tape-casting process. Compared with that of the bulk ceramics, the thickness of single layer is reduced from ~200 to ~20 μm. The E_b is thus increased from 200 to 720 kV/cm (Figs. 24(a) and 24(b)). The decreased thickness reduces the probability of defects. With the substantial increment in E_b, the W_{rec} also elevates from 2.5 to 9.5 J/cm^3 and still maintains an ultra-high η of 90%.

Later, Li *et al*. [57] combined the tape-casting process with texture engineering to construct <111>-textured NBT–0.35SBT MLCCs. Ceramic capacitors will generate strain and elastic energy under an external electric field, which may result in the electromechanical breakdown [189]. The electrostriction of perovskite structures generally exhibits obvious anisotropy. In particular, the electrostriction strain coefficient in the <100> directions is about 4–5 times larger than that in the <111> directions [190]. Under an electric field of 50 MV/m, the strain of <111>-textured ceramics is only 0.19%, which is much reduced compared with that of nontextured ceramics (0.55%) (Fig. 24(c)). Benefiting from the much reduced strain, the E_b of <111>-textured ceramics achieves 103 MV/m, which is 61% higher than that of nontextured ceramics (~64 MV/m) (Fig. 24(d)). The multi-scale synergic optimization of elemental modification, texture engineering, and tape-casting process plays a very important role in optimizing the energy storage properties. The W_{rec} of ~21.5 J/cm^3 with η of ~80% is realized in <111>-textured ceramics, which is 1.5 times larger than that of the nontextured counterparts (Figs. 24(e) and 24(f)).

Zhu *et al*. [23] reported the ANT+0.25 wt% MnO_2 MLCCs with the ultra-high E_b by adjusting the thickness of active and inactive layers. Ultimately, due

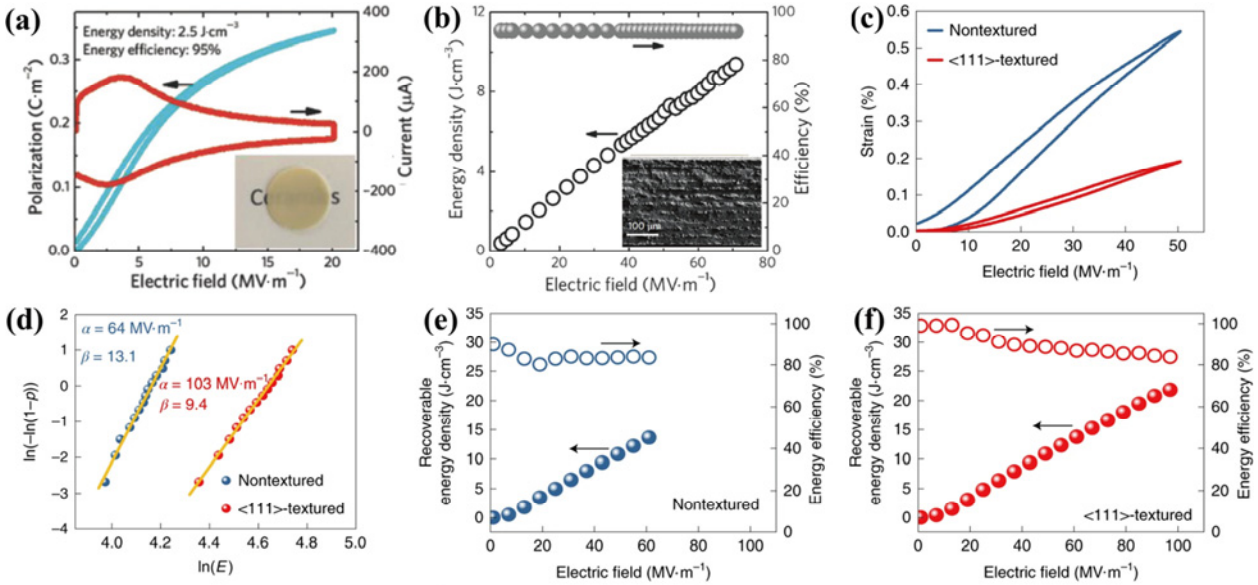

Fig. 24 *P*–*E* loops of (a) 0.55NBT–0.45SBT bulk ceramics and (b) 0.55NBT–0.45SBT MLCCs. (c) Strain vs. electric field curves and (d) E_b of <111>-textured and nontextured MLCCs. Energy storage performance of (e) nontextured and (f) <111>-textured multilayer ceramics. Reproduced with permission from Ref. [5] for (a, b), © WILEY-VCH Verlag GmbH & Co. KGaA, Weinheim 2018; Ref. [57] for (c–f), © The Author(s), under exclusive licence to Springer Nature Limited 2020.

to the small grain size, low leakage current, and thin thickness, the E_b of 1020 kV/cm is achieved, 343% larger than that of bulk ceramics [23,34]. The energy density is accordingly increased from 4.2 to 7.9 J/cm^3.

The decreased dielectric layer thickness induced by the tape-casting process is the main reason for the enhancement of E_b. MLCCs prepared via the tape-casting process are one of the most widely used method for commercial ceramic capacitors [58,191,192]. Zhao *et al*. [193] prepared an RFE multilayer energy storage ceramic capacitor (MLESCC) of 0.87BT–0.13BZNT with a dielectric layer thickness of 5 μm. The E_b is increased to 1060 kV/cm, and W_{rec} is increased to 10.12 J/cm^3. Later, they combined tape-casting process with a core–shell structure to prepare a BT–BZNT@SiO_2 MLCC with E_b up to 175.5 MV/m and the giant W_{rec} of 18.24 J/cm^3 with ultra-high η of 94.5% [58]. With the help of decreased dielectric layer thickness, E_b of $(Pb_{0.875}La_{0.05}Sr_{0.05})$ $(Zr_{0.695}Ti_{0.005}Sn_{0.3})O_3$ (PLSZTS) is also increased from 555 kV/cm (bulk) to 850 kV/cm (MLCC). The ultrahigh W_{rec} of 19.2 J/cm^3 and η of 96.4% are therefore obtained [194].

3. 5 Multi-scale synergic optimization

In the previous sections, it can be seen that the modification strategies at various scales play their distinct roles in enhancing the energy storage performance. And it is rational to anticipate that the synergetic modifications at multi-scales can boom the energy storage potential of dielectrics better. Take the multi-scale modifications of BT–BZNT MLCC as an example [195]. At the nanoscale, RFE BT ceramics can be obtained by introducing BZNT; at the mesoscale, the reduced grain sizes are achieved via two-step sintering and at the macroscale, and the tape-casting process can reduce the thickness of the single layer of dielectrics. With the combination of the above effects, the E_b up to 750 kV/cm and the high W_{rec} of 8.13 J/cm^3 with ultra-high η of 95% were finally achieved. Wang *et al*. [188] also successfully obtained high-performance BT–BZNT@SiO_2 MLCC via combining the above effects and the core–shell structure, in which giant W_{rec} of 18.24 J/cm^3 and η of 94.5% were obtained under a large electric field of 1755 kV/cm. Wang *et al*. [196] used Al_2O_3 and SiO_2 to wrap BT powders to build the core–shell structure. Meanwhile, the tape-casting process was utilized to reduce the single layer thickness of the ceramic from 63 to 12 μm. As a result, the E_b of the BT@(Al_2O_3+SiO_2) MLCC was increased from 184 to 665 kV/cm, giving rise to the > 250% enhancement in W_{rec} (i.e., from 1.14 to 4.06 J/cm^3).

In addition, there are many other combinations of multi-scale optimization strategies, including but not limited to the phase engineering combined with high-energy ball milling [33], the synergic modulations involving the hydrothermal synthesis, phase engineering, and constructing core–shell structure [27], and the comprehensive optimization of domain engineering combined with two-step sintering [164].

4 Summary and perspectives

The modification methods at different scales have their own characteristics. Figure 25 summarizes the typical modification methods for ceramics reported so far [23,28,47,48,52,58,62,64,71,73,75,95,103,116,117,119,130,141,142,156,164,172,181,193,194,197–212]. With the continuous development of electronic information technology, the demand for dielectric capacitors in the

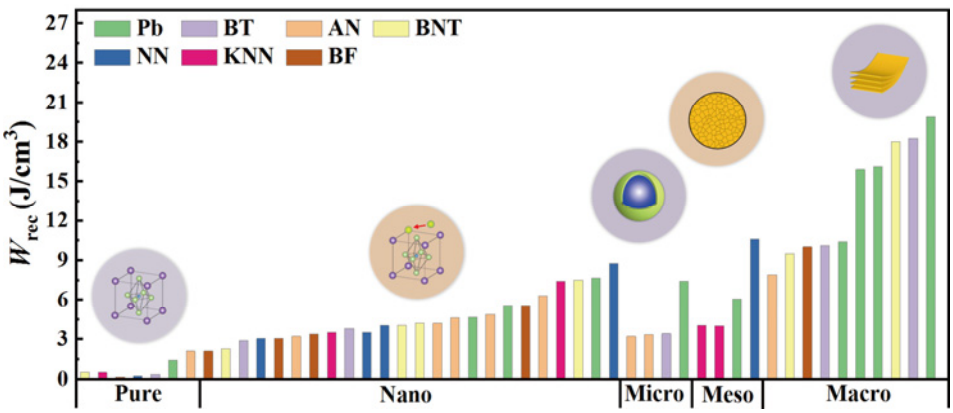

Fig. 25 W_{rec} of energy storage ceramics after modification by different methods.

field of high-power/pulsed devices is increasing. Ideal energy storage capacitors need to possess high polarization, low loss, and large E_b. This review summarizes the multi-scale modification strategies of ceramics from the nanoscale, microscale, mesoscale, and macroscale and lists some common features.

1) At the nanoscale: Modulating the phase and domain structures via doping or forming solid solutions is a simple and effective method. Ceramics normally have a variety of complex phase structures, which accordingly give rise to different performance. The energy storage property is often optimized by stable AFE phase regions (the AFE_O phase region in PLZT ceramics), relaxor phase boundaries (the M_2–M_3 phase boundary in AN ceramics), etc. Domain engineering is usually achieved via the nanoscale PNRs. These nanodomains are sensitive to the external electric field, which can reduce hysteresis and improve the energy efficiency. Moreover, the energy storage performance can be improved by special elements that can enhance the E_g (CH) or polarization (Bi^{3+} and W^{6+}).

2) At the microscale: The "core–shell" structure was constructed via depositing a coating layer with low dielectric constants (such as SiO_2 and ST) on the ceramic grains, which can improve the E_b, maintain the high polarization, and finally reach excellent energy storage properties.

3) At the mesoscale: There is a strong link between the ceramic grain size and E_b, that is, E_b increases exponentially with the decreased grain size. Therefore, the preparation of fine-grain ceramics via high-energy ball milling, two-step sintering, or hydrothermal synthesis can significantly optimize the E_b and improve the energy density. Constructing 0–3 type composites through interface design can also enhance the energy storage performance.

4) At the macroscale: The rolling process can greatly improve the relative density of the ceramics, and the tape-casting process can reduce the monolayer thickness down to < 50 μm, which would greatly facilitate the E_b. It also enables the stacking of multilayer ceramics to achieve the integration of ceramic capacitor devices and enhances the practical application capability.

In addition, ceramic films serving as a special kind of high energy storage material show great potential for high E_b and W_{rec} due to the reduced thickness (< 1 μm) and the formation of polymorphic nanodomains. Up to now, extensive efforts have been paid on dielectric ceramic films, and the W_{rec} of 50–300 J/cm^3, η of 60%–90%, E_b of 1–6 MV/cm, and thermal stability over the range of −50–200 ℃ have been successfully achieved. And better comprehensive energy storage performance is highly anticipated with the development of large-area epitaxial film deposition. Moreover, the thick films and multilayered films can also be explored to further enhance the energy density. Ceramic films are becoming a rising star in the dielectric energy storage ceramics.

With the great effects of many research groups for decades, ceramic capacitors have achieved significantly excellent energy storage properties, but there are still many challenges. For example, the failure mechanism under long-term cyclic operation is still not clear. Especially, the generated thermal energy and mechanical energy during the charge/discharge cycling will seriously affect the performance and service life of capacitors. Therefore, it is important and urgent to study the failure mechanism of dielectric capacitors under multi-field including but not limited to force, electric, and thermal coupling conditions in long-term cyclic operation.

Acknowledgements

This work was supported by the National Natural Science Foundation of China (52073144 and 12004181), the Natural Science Foundation of Jiangsu Province (BK20201301 and BK20200473), State Key Laboratory of New Ceramics and Fine Processing, Tsinghua University (KF202114), the Research Fund of State Key Laboratory of Mechanics and Control of Mechanical Structures, Nanjing University of Aeronautics and Astronautics (MCMS-I-0522G02), and a Project Funded by a project of the Priority Academic Program Development (PAPD) of Jiangsu Higher Education Institutions.

Declaration of competing interest

The authors have no competing interests to declare that are relevant to the content of this article.

References

[1] Ibn-Mohammed T, Randall CA, Mustapha KB, *et al*. Decarbonising ceramic manufacturing: A techno-economic analysis of energy efficient sintering technologies in the functional materials sector. *J Eur Ceram Soc* 2019, **39**: 5213–5235.

[2] Wang G, Lu ZL, Li Y, *et al*. Electroceramics for high-energy density capacitors: Current status and future perspectives. *Chem Rev* 2021, **121**: 6124–6172.
[3] Sherrill SA, Banerjee P, Rubloff GW, *et al*. High to ultra-high power electrical energy storage. *Phys Chem Chem Phys* 2011, **13**: 20714–20723.
[4] Liu C, Li F, Ma LP, *et al*. Advanced materials for energy storage. *Adv Mater* 2010, **22**: E28–E62.
[5] Li JL, Li F, Xu Z, *et al*. Multilayer lead-free ceramic capacitors with ultrahigh energy density and efficiency. *Adv Mater* 2018, **30**: 1802155.
[6] Lee H, Kim JR, Lanagan MJ, *et al*. High-energy density dielectrics and capacitors for elevated temperatures: $Ca(Zr,Ti)O_3$. *J Am Ceram Soc* 2013, **96**: 1209–1213.
[7] Prateek, Thakur VK, Gupta RK. Recent progress on ferroelectric polymer-based nanocomposites for high energy density capacitors: Synthesis, dielectric properties, and future aspects. *Chem Rev* 2016, **116**: 4260–4317.
[8] Yao ZH, Song Z, Hao H, *et al*. Homogeneous/inhomogeneous-structured dielectrics and their energy-storage performances. *Adv Mater* 2017, **29**: 1601727.
[9] Han FM, Meng GW, Zhou F, *et al*. Dielectric capacitors with three-dimensional nanoscale interdigital electrodes for energy storage. *Sci Adv* 2015, **1**: e1500605.
[10] Dang ZM, Yuan JK, Yao SH, *et al*. Flexible nanodielectric materials with high permittivity for power energy storage. *Adv Mater* 2013, **25**: 6334–6365.
[11] Palneedi H, Peddigari M, Hwang GT, *et al*. High- performance dielectric ceramic films for energy storage capacitors: Progress and outlook. *Adv Funct Mater* 2018, **28**: 1803665.
[12] Ibrahim H, Ilinca A, Perron J. Energy storage systems—Characteristics and comparisons. *Renew Sust Energ Rev* 2008, **12**: 1221–1250.
[13] Pan H, Lan S, Xu SQ, *et al*. Ultrahigh energy storage in superparaelectric relaxor ferroelectrics. *Science* 2021, **374**: 100–104.
[14] Pan H, Li F, Liu Y, *et al*. Ultrahigh-energy density lead-free dielectric films via polymorphic nanodomain design. *Science* 2019, **365**: 578–582.
[15] Burn I, Smyth DM. Energy storage in ceramic dielectrics. *J Mater Sci* 1972, **7**: 339–343.
[16] Chauhan A, Patel S, Vaish R, *et al*. Anti-ferroelectric ceramics for high energy density capacitors. *Materials* 2015, **8**: 8009–8031.
[17] Zhao PY, Cai ZM, Wu LW, *et al*. Perspectives and challenges for lead-free energy-storage multilayer ceramic capacitors. *J Adv Ceram* 2021, **10**: 1153–1193.
[18] Li B, Liu QX, Tang XG, *et al*. Antiferroelectric to relaxor ferroelectric phase transition in PbO modified $(Pb_{0.97}La_{0.02})(Zr_{0.95}Ti_{0.05})O_3$ ceramics with a large energy-density for dielectric energy storage. *RSC Adv* 2017, **7**: 43327–43333.
[19] Jiang J, Li XJ, Li L, *et al*. Novel lead-free $NaNbO_3$-based relaxor antiferroelectric ceramics with ultrahigh energy storage density and high efficiency. *J Materiomics* 2022, **8**: 295–301.
[20] Li DX, Zeng XJ, Li ZP, *et al*. Progress and perspectives in dielectric energy storage ceramics. *J Adv Ceram* 2021, **10**: 675–703.
[21] Wang J, Rao Y, Fan XH, *et al*. Synergic modulation of over-stoichiometrical MnO_2 and SiO_2-coated particles on the energy storage properties of silver niobate-based ceramics. *Ceram Int* 2021, **47**: 19595–19604.
[22] Wang J, Wan XH, Rao Y, *et al*. Hydrothermal synthesized $AgNbO_3$ powders: Leading to greatly improved electric breakdown strength in ceramics. *J Eur Ceram Soc* 2020, **40**: 5589–5596.
[23] Zhu LF, Zhao L, Yan YK, *et al*. Composition and strain engineered $AgNbO_3$-based multilayer capacitors for ultra-high energy storage capacity. *J Mater Chem A* 2021, **9**: 9655–9664.
[24] Qi H, Xie AW, Tian A, *et al*. Superior energy-storage capacitors with simultaneously giant energy density and efficiency using nanodomain engineered $BiFeO_3$–$BaTiO_3$–$NaNbO_3$ lead-free bulk ferroelectrics. *Adv Energy Mater* 2020, **10**: 1903338.
[25] Yang LT, Kong X, Li F, *et al*. Perovskite lead-free dielectrics for energy storage applications. *Prog Mater Sci* 2019, **102**: 72–108.
[26] Ma JJ, Zhang J, Guo J, *et al*. Achieving ultrahigh energy storage density in lead-free sodium niobate-based ceramics by modulating the antiferroelectric phase. *Chem Mater* 2022, **34**: 7313–7322.
[27] Fan XH, Wang J, Yuan H, *et al*. Synergic enhancement of energy storage density and efficiency in MnO_2-doped $AgNbO_3$@SiO_2 ceramics via A/B-site substitutions. *ACS Appl Mater Interfaces* 2022, **14**: 7052–7062.
[28] Yuan QB, Yao FZ, Cheng SD, *et al*. Bioinspired hierarchically structured all-inorganic nanocomposites with significantly improved capacitive performance. *Adv Funct Mater* 2020, **30**: 2000191.
[29] Chen L, Long FX, Qi H, *et al*. Outstanding energy storage performance in high-hardness $(Bi_{0.5}K_{0.5})TiO_3$-based lead-free relaxors via multi-scale synergistic design. *Adv Funct Mater* 2022, **32**: 2110478.
[30] Fan XH, Wang J, Rao Y, *et al*. Simultaneous improved polarization and breakdown strength in Mn/W co-doped silver niobate ceramics. *J Mater Sci* 2021, **56**: 19155–19164.
[31] Lu ZL, Bao WC, Wang G, *et al*. Mechanism of enhanced energy storage density in $AgNbO_3$-based lead-free antiferroelectrics. *Nano Energy* 2021, **79**: 105423.
[32] Yuan QB, Li G, Yao FZ, *et al*. Simultaneously achieved temperature-insensitive high energy density and efficiency in domain engineered $BaTiO_3$–$Bi(Mg_{0.5}Zr_{0.5})O_3$ lead-free relaxor ferroelectrics. *Nano Energy* 2018, **52**: 203–210.
[33] Chen L, Deng SQ, Liu H, *et al*. Giant energy-storage density with ultrahigh efficiency in lead-free relaxors via high-entropy design. *Nat Commun* 2022, **13**: 3089.
[34] Zhao L, Liu Q, Gao J, *et al*. Lead-free antiferroelectric

silver niobate tantalate with high energy storage performance. *Adv Mater* 2017, **29**: 1701824.

[35] Cui T, Zhang J, Guo J, *et al*. Simultaneous achievement of ultrahigh energy storage density and high efficiency in $BiFeO_3$-based relaxor ferroelectric ceramics via a highly disordered multicomponent design. *J Mater Chem A* 2022, **10**: 14316–14325.

[36] Hanzig J, Zschornak M, Nentwich M, *et al*. Strontium titanate: An all-in-one rechargeable energy storage material. *J Power Sources* 2014, **267**: 700–705.

[37] Bartkowiak M, Mahan GD. Nonlinear currents in Voronoi networks. *Phys Rev B* 1995, **51**: 10825–10832.

[38] Shay DP, Podraza NJ, Donnelly NJ, *et al*. High energy density, high temperature capacitors utilizing Mn-doped $0.8CaTiO_3$–$0.2CaHfO_3$ ceramics. *J Am Ceram Soc* 2012, **95**: 1348–1355.

[39] Shende RV, Krueger DS, Rossetti GA, *et al*. Strontium zirconate and strontium titanate ceramics for high-voltage applications: Synthesis, processing, and dielectric properties. *J Am Ceram Soc* 2001, **84**: 1648–1650.

[40] Song Z, Liu HX, Zhang SJ, *et al*. Effect of grain size on the energy storage properties of $(Ba_{0.4}Sr_{0.6})TiO_3$ paraelectric ceramics. *J Eur Ceram Soc* 2014, **34**: 1209–1217.

[41] Li JJ, Claude J, Norena-Franco LE, *et al*. Electrical energy storage in ferroelectric polymer nanocomposites containing surface-functionalized $BaTiO_3$ nanoparticles. *Chem Mater* 2008, **20**: 6304–6306.

[42] Tang HX, Zhou Z, Sodano HA. Large-scale synthesis of $Ba_xSr_{1-x}TiO_3$ nanowires with controlled stoichiometry. *Appl Phys Lett* 2014, **104**: 142905.

[43] Zhou Z, Tang HX, Sodano HA. Scalable synthesis of morphotropic phase boundary lead zirconium titanate nanowires for energy harvesting. *Adv Mater* 2014, **26**: 7547–7554.

[44] Cui T, Yu AN, Zhang YY, *et al*. Energy storage performance of $BiFeO_3$–$SrTiO_3$–$BaTiO_3$ relaxor ferroelectric ceramics. *J Am Ceram Soc* 2022, **105**: 6252–6261.

[45] Randall CA, Fan ZM, Reaney I, *et al*. Antiferroelectrics: History, fundamentals, crystal chemistry, crystal structures, size effects, and applications. *J Am Ceram Soc* 2021, **104**: 3775–3810.

[46] Jaffe B. Antiferroelectric ceramics with field-enforced transitions: A new nonlinear circuit element. *Proc IRE* 1961, **49**: 1264–1267.

[47] Ji HF, Wang DW, Bao WC, *et al*. Ultrahigh energy density in short-range tilted NBT-based lead-free multilayer ceramic capacitors by nanodomain percolation. *Energy Storage Mater* 2021, **38**: 113–120.

[48] Wang HS, Liu YC, Yang TQ, *et al*. Ultrahigh energy-storage density in antiferroelectric ceramics with field-induced multiphase transitions. *Adv Funct Mater* 2019, **29**: 1807321.

[49] Ma JJ, Zhang DH, Ying F, *et al*. Ultrahigh energy storage density and high efficiency in lead-free $(Bi_{0.9}Na_{0.1})(Fe_{0.8}Ti_{0.2})O_3$-modified $NaNbO_3$ ceramics via stabilizing the antiferroelectric phase and enhancing relaxor behavior. *ACS Appl Mater Interfaces* 2022, **14**: 19704–19713.

[50] Zhang MH, Hadaeghi N, Egert S, *et al*. Design of lead-free antiferroelectric $(1-x)NaNbO_3$–$xSrSnO_3$ compositions guided by first-principles calculations. *Chem Mater* 2021, **33**: 266–274.

[51] Dong XY, Li X, Chen HY, *et al*. Realizing enhanced energy storage and hardness performances in $0.90NaNbO_3$–$0.10Bi(Zn_{0.5}Sn_{0.5})O_3$ ceramics. *J Adv Ceram* 2022, **11**: 729–741.

[52] Luo NN, Han K, Cabral MJ, *et al*. Constructing phase boundary in $AgNbO_3$ antiferroelectrics: Pathway simultaneously achieving high energy density and efficiency. *Nat Commun* 2020, **11**: 4824.

[53] Qi H, Zuo RZ. Linear-like lead-free relaxor antiferroelectric $(Bi_{0.5}Na_{0.5})TiO_3$–$NaNbO_3$ with giant energy-storage density/efficiency and super stability against temperature and frequency. *J Mater Chem A* 2019, **7**: 3971–3978.

[54] Jiang J, Meng XJ, Li L, *et al*. Ultrahigh energy storage density in lead-free relaxor antiferroelectric ceramics via domain engineering. *Energy Storage Mater* 2021, **43**: 383–390.

[55] Fu DS, Endo M, Taniguchi H, *et al*. $AgNbO_3$: A lead-free material with large polarization and electromechanical response. *Appl Phys Lett* 2007, **90**: 252907.

[56] Gallagher JA, Jo HR, Lynch CS. Large-field dielectric loss in relaxor ferroelectric PLZT. *Smart Mater Struct* 2014, **23**: 035007.

[57] Li JL, Shen ZH, Chen XH, *et al*. Grain-orientation-engineered multilayer ceramic capacitors for energy storage applications. *Nat Mater* 2020, **19**: 999–1005.

[58] Zhao PY, Cai ZM, Chen LL, *et al*. Ultra-high energy storage performance in lead-free multilayer ceramic capacitors via a multiscale optimization strategy. *Energy Environ Sci* 2020, **13**: 4882–4890.

[59] Zhao PY, Chen LL, Li LT, *et al*. Ultrahigh energy density with excellent thermal stability in lead-free multilayer ceramic capacitors via composite strategy design. *J Mater Chem A* 2021, **9**: 25914–25921.

[60] Kim C, Pilania G, Ramprasad R. Machine learning assisted predictions of intrinsic dielectric breakdown strength of ABX_3 perovskites. *J Phys Chem C* 2016, **120**: 14575–14580.

[61] Xu YH, Yang ZD, Xu K, *et al*. Modulated band structure and phase transitions in calcium hafnate titanate modified silver niobate ceramics for energy storage. *Chem Eng J* 2021, **426**: 131047.

[62] Luo CY, Feng Q, Luo NN, *et al*. Effect of Ca^{2+}/Hf^{4+} modification at A/B sites on energy-storage density of $Bi_{0.47}Na_{0.47}Ba_{0.06}TiO_3$ ceramics. *Chem Eng J* 2021, **420**: 129861.

[63] Li S, Hu TF, Nie HC, *et al*. Giant energy density and high efficiency achieved in silver niobate-based lead-free antiferroelectric ceramic capacitors via domain engineering. *Energy Storage Mater* 2021, **34**: 417–426.

[64] Dai ZH, Xie JL, Chen ZB, *et al*. Improved energy storage density and efficiency of $(1-x)Ba_{0.85}Ca_{0.15}Zr_{0.1}Ti_{0.9}O_3$–$xBiMg_{2/3}Nb_{1/3}O_3$ lead-free ceramics. *Chem Eng J* 2021, **410**: 128341.

[65] Luo NN, Han K, Zhuo FP, *et al*. Aliovalent A-site engineered $AgNbO_3$ lead-free antiferroelectric ceramics toward superior energy storage density. *J Mater Chem A* 2019, **7**: 14118–14128.

[66] Jin Q, Zhao LL, Cui B, *et al*. Enhanced energy storage properties in lead-free $BaTiO_3$@$Na_{0.5}K_{0.5}NbO_3$ nano-ceramics with nanodomains via a core–shell structural design. *J Mater Chem C* 2020, **8**: 5248–5258.

[67] Fan PY, Zhang ST, Xu JW, *et al*. Relaxor/antiferroelectric composites: A solution to achieve high energy storage performance in lead-free dielectric ceramics. *J Mater Chem C* 2020, **8**: 5681–5691.

[68] You D, Tan H, Yan ZL, *et al*. Enhanced dielectric energy storage performance of $0.45Na_{0.5}Bi_{0.5}TiO_3$–$0.55Sr_{0.7}Bi_{0.2}TiO_3$/AlN 0–3 type lead-free composite ceramics. *ACS Appl Mater Interfaces* 2022, **14**: 17652–17661.

[69] Li F, Hou X, Wang J, *et al*. Structure-design strategy of 0–3 type $(Bi_{0.32}Sr_{0.42}Na_{0.20})TiO_3$/MgO composite to boost energy storage density, efficiency and charge–discharge performance. *J Eur Ceram Soc* 2019, **39**: 2889–2898.

[70] Tao CW, Geng XY, Zhang J, *et al*. $Bi_{0.5}Na_{0.5}TiO_3$–$BaTiO_3$–$K_{0.5}Na_{0.5}NbO_3$:ZnO relaxor ferroelectric composites with high breakdown electric field and large energy storage properties. *J Eur Ceram Soc* 2018, **38**: 4946–4952.

[71] Zhang YM, Cao MH, Yao ZH, *et al*. Effects of silica coating on the microstructures and energy storage properties of $BaTiO_3$ ceramics. *Mater Res Bull* 2015, **67**: 70–76.

[72] Huang YH, Wu YJ, Qiu WJ, *et al*. Enhanced energy storage density of $Ba_{0.4}Sr_{0.6}TiO_3$–MgO composite prepared by spark plasma sintering. *J Eur Ceram Soc* 2015, **35**: 1469–1476.

[73] Yu Z, Zeng JT, Zheng LY, *et al*. Microstructure effects on the energy storage density in $BiFeO_3$-based ferroelectric ceramics. *Ceram Int* 2021, **47**: 12735–12741.

[74] Ding JX, Liu YF, Lu YN, *et al*. Enhanced energy-storage properties of $0.89Bi_{0.5}Na_{0.5}TiO_3$–$0.06BaTiO_3$–$0.05K_{0.5}Na_{0.5}NbO_3$ lead-free anti-ferroelectric ceramics by two-step sintering method. *Mater Lett* 2014, **114**: 107–110.

[75] Huang J, Hou X, Gao SB, *et al*. Greatly enhanced energy storage and discharge properties of $AgNbO_3$ ceramics with a stable antiferroelectric phase and high breakdown strength using hydrothermally synthesized powders. *J Mater Chem A* 2022, **10**: 16337–16350.

[76] Borkar H, Singh VN, Singh BP, *et al*. Room temperature lead-free relaxor-antiferroelectric electroceramics for energy storage applications. *RSC Adv* 2014, **4**: 22840–22847.

[77] Wang XC, Yang TQ, Shen J. High-energy storage performance in $(Pb_{0.98}La_{0.02})(Zr_{0.45}Sn_{0.55})_{0.995}O_3$ AFE thick films fabricated via a rolling process. *J Am Ceram Soc* 2016, **99**: 3569–3572.

[78] Su B, Button TW. A comparative study of viscous polymer processed ceramics based on aqueous and non-aqueous binder systems. *J Mater Process Technol* 2009, **209**: 153–157.

[79] Jiang J, Meng XJ, Li L, *et al*. Enhanced energy storage properties of lead-free $NaNbO_3$-based ceramics via A/B-site substitution. *Chem Eng J* 2021, **422**: 130130.

[80] Li DX, Shen ZY, Li ZP, *et al*. *P–E* hysteresis loop going slim in $Ba_{0.3}Sr_{0.7}TiO_3$-modified $Bi_{0.5}Na_{0.5}TiO_3$ ceramics for energy storage applications. *J Adv Ceram* 2020, **9**: 183–192.

[81] Jo HR, Lynch CS. A high energy density relaxor antiferroelectric pulsed capacitor dielectric. *J Appl Phys* 2016, **119**: 024104.

[82] Liu Z, Lu T, Ye JM, *et al*. Antiferroelectrics for energy storage applications: A review. *Adv Mater Technol* 2018, **3**: 1800111.

[83] Pan WY, Zhang QM, Bhalla A, *et al*. Field-forced antiferroelectric-to-ferroelectric switching in modified lead zirconate titanate stannate ceramics. *J Am Ceram Soc* 1989, **72**: 571–578.

[84] Liu ZG, Li MD, Tang ZH, *et al*. Enhanced energy storage density and efficiency in lead-free $Bi(Mg_{1/2}Hf_{1/2})O_3$-modified $BaTiO_3$ ceramics. *Chem Eng J* 2021, **418**: 129379.

[85] Cui T, Zhang J, Guo J, *et al*. Outstanding comprehensive energy storage performance in lead-free $BiFeO_3$-based relaxor ferroelectric ceramics by multiple optimization design. *Acta Mater* 2022, **240**: 118286.

[86] Shrout TR, Zhang SJ. Lead-free piezoelectric ceramics: Alternatives for PZT? *J Electroceram* 2007, **19**: 185.

[87] Gao JH, Liu YB, Wang Y, *et al*. High temperature-stability of $(Pb_{0.9}La_{0.1})(Zr_{0.65}Ti_{0.35})O_3$ ceramic for energy-storage applications at finite electric field strength. *Scripta Mater* 2017, **137**: 114–118.

[88] Li B, Liu QX, Tang XG, *et al*. High energy storage density and impedance response of PLZT2/95/5 antiferroelectric ceramics. *Materials* 2017, **10**: 143.

[89] Qiao PX, Zhang YF, Chen XF, *et al*. Enhanced energy storage properties and stability in $(Pb_{0.895}La_{0.07})(Zr_xTi_{1-x})O_3$ antiferroelectric ceramics. *Ceram Int* 2019, **45**: 15898–15905.

[90] Chen SC, Wang XC, Yang TQ, *et al*. Composition-dependent dielectric properties and energy storage performance of $(Pb,La)(Zr,Sn,Ti)O_3$ antiferroelectric ceramics. *J Electroceram* 2014, **32**: 307–310.

[91] Wang XC, Shen J, Yang TQ, *et al*. High energy-storage performance and dielectric properties of antiferroelectric $(Pb_{0.97}La_{0.02})(Zr_{0.5}Sn_{0.5-x}Ti_x)O_3$ ceramic. *J Alloys Compd* 2016, **655**: 309–313.

[92] Shen J, Wang XC, Yang TQ, *et al*. High discharge energy density and fast release speed of $(Pb,La)(Zr,Sn,Ti)O_3$ antiferroelectric ceramics for pulsed capacitors. *J Alloys Compd* 2017, **721**: 191–198.

[93] Dan Y, Xu HJ, Zou KL, *et al*. Energy storage characteristics of (Pb,La)(Zr,Sn,Ti)O_3 antiferroelectric ceramics with high Sn content. *Appl Phys Lett* 2018, **113**: 063902.

[94] Liu XH, Li Y, Hao XH. Ultra-high energy-storage density and fast discharge speed of $(Pb_{0.98-x}La_{0.02}Sr_x)(Zr_{0.9}Sn_{0.1})_{0.995}O_3$ antiferroelectric ceramics prepared via the tape-casting method. *J Mater Chem A* 2019, **7**: 11858–11866.

[95] Zhang QF, Tong HF, Chen J, *et al*. High recoverable energy density over a wide temperature range in Sr modified (Pb,La)(Zr,Sn,Ti)O_3 antiferroelectric ceramics with an orthorhombic phase. *Appl Phys Lett* 2016, **109**: 262901.

[96] Dai XH, Xu Z, Li JF, *et al*. Effects of lanthanum modification on rhombohedral $Pb(Zr_{1-x}Ti_x)O_3$ ceramics: Part II. Relaxor behavior versus enhanced antiferroelectric stability. *J Mater Res* 1996, **11**: 626–638.

[97] Markowski K, Park SE, Yoshikawa S, *et al*. Effect of compositional variations in the lead lanthanum zirconate stannate titanate system on electrical properties. *J Am Ceram Soc* 1996, **79**: 3297–3304.

[98] Peláiz-Barranco A, Guerra JDS, García-Zaldívar O, *et al*. Effects of lanthanum modification on dielectric properties of $Pb(Zr_{0.90},Ti_{0.10})O_3$ ceramics: Enhanced antiferroelectric stability. *J Mater Sci* 2008, **43**: 6087–6093.

[99] Zhuo FP, Li Q, Li YY, *et al*. Effect of A-site La^{3+} modified on dielectric and energy storage properties in lead zironate stannate titanate ceramics. *Mater Res Express* 2014, **1**: 045501.

[100] Liu Z, Bai Y, Chen XF, *et al*. Linear composition-dependent phase transition behavior and energy storage performance of tetragonal PLZST antiferroelectric ceramics. *J Alloys Compd* 2017, **691**: 721–725.

[101] Chen SC, Yang TQ, Wang JF, *et al*. Effects of glass additions on the dielectric properties and energy storage performance of $Pb_{0.97}La_{0.02}(Zr_{0.56}Sn_{0.35}Ti_{0.09})O_3$ antiferroelectric ceramics. *J Mater Sci-Mater El* 2013, **24**: 4764–4768.

[102] Tian Y, Jin L, Zhang HF, *et al*. Phase transitions in bismuth-modified silver niobate ceramics for high power energy storage. *J Mater Chem A* 2017, **5**: 17525–17531.

[103] Tian Y, Jin L, Zhang HF, *et al*. High energy density in silver niobate ceramics. *J Mater Chem A* 2016, **4**: 17279–17287.

[104] Pawełczyk M. Phase transitions in $AgTa_xNb_{1-x}O_3$ solid solutions. *Phase Transit* 1987, **8**: 273–292.

[105] Luo NN, Han K, Liu LJ, *et al*. Lead-free $Ag_{1-3x}La_xNbO_3$ antiferroelectric ceramics with high-energy storage density and efficiency. *J Am Ceram Soc* 2019, **102**: 4640–4647.

[106] Shi P, Wang XJ, Lou XJ, *et al*. Significantly enhanced energy storage properties of Nd^{3+} doped $AgNbO_3$ lead-free antiferroelectric ceramics. *J Alloys Compd* 2021, **877**: 160162.

[107] Li S, Nie HC, Wang GS, *et al*. Significantly enhanced energy storage performance of rare-earth-modified silver niobate lead-free antiferroelectric ceramics via local chemical pressure tailoring. *J Mater Chem C* 2019, **7**: 1551–1560.

[108] Han K, Luo NN, Mao SF, *et al*. Realizing high low-electric-field energy storage performance in $AgNbO_3$ ceramics by introducing relaxor behaviour. *J Materiomics* 2019, **5**: 597–605.

[109] Gao J, Zhang YC, Zhao L, *et al*. Enhanced antiferroelectric phase stability in La-doped $AgNbO_3$: Perspectives from the microstructure to energy storage properties. *J Mater Chem A* 2019, **7**: 2225–2232.

[110] Mao SF, Luo NN, Han K, *et al*. Effect of Lu doping on the structure, electrical properties and energy storage performance of $AgNbO_3$ antiferroelectric ceramics. *J Mater Sci-Mater El* 2020, **31**: 7731–7741.

[111] Yang ZT, Gao F, Du HL, *et al*. Grain size engineered lead-free ceramics with both large energy storage density and ultrahigh mechanical properties. *Nano Energy* 2019, **58**: 768–777.

[112] Shao TQ, Du HL, Ma H, *et al*. Potassium-sodium niobate based lead-free ceramics: Novel electrical energy storage materials. *J Mater Chem A* 2017, **5**: 554–563.

[113] Tao H, Wu HJ, Liu Y, *et al*. Ultrahigh performance in lead-free piezoceramics utilizing a relaxor slush polar state with multiphase coexistence. *J Am Chem Soc* 2019, **141**: 13987–13994.

[114] Gao XL, Li Y, Chen JW, *et al*. High energy storage performances of $Bi_{1-x}Sm_xFe_{0.95}Sc_{0.05}O_3$ lead-free ceramics synthesized by rapid hot press sintering. *J Eur Ceram Soc* 2019, **39**: 2331–2338.

[115] Wang DW, Fan ZM, Zhou D, *et al*. Bismuth ferrite-based lead-free ceramics and multilayers with high recoverable energy density. *J Mater Chem A* 2018, **6**: 4133–4144.

[116] Qi H, Zuo RZ, Xie AW, *et al*. Ultrahigh energy-storage density in $NaNbO_3$-based lead-free relaxor antiferroelectric ceramics with nanoscale domains. *Adv Funct Mater* 2019, **29**: 1903877.

[117] Xu CH, Fu ZQ, Liu Z, *et al*. La/Mn codoped $AgNbO_3$ lead-free antiferroelectric ceramics with large energy density and power density. *ACS Sustainable Chem Eng* 2018, **6**: 16151–16159.

[118] Gao J, Liu Q, Dong JF, *et al*. Local structure heterogeneity in Sm-doped $AgNbO_3$ for improved energy-storage performance. *ACS Appl Mater Interfaces* 2020, **12**: 6097–6104.

[119] Yan ZN, Zhang D, Zhou XF, *et al*. Silver niobate based lead-free ceramics with high energy storage density. *J Mater Chem A* 2019, **7**: 10702–10711.

[120] Zhu XP, Gao YF, Shi P, *et al*. Ultrahigh energy storage density in $(Bi_{0.5}Na_{0.5})_{0.65}Sr_{0.35}TiO_3$-based lead-free relaxor ceramics with excellent temperature stability. *Nano Energy* 2022, **98**: 107276.

[121] Chu BJ, Zhou X, Ren KL, *et al*. A dielectric polymer with high electric energy density and fast discharge speed. *Science* 2006, **313**: 334–336.

[122] Love GR. Energy storage in ceramic dielectrics. *J Am Ceram Soc* 1990, **73**: 323–328.
[123] Shen Y, Zhang X, Li M, *et al*. Polymer nanocomposite dielectrics for electrical energy storage. *Natl Sci Rev* 2017, **4**: 23–25.
[124] Tanaka T, Greenwood A. Effects of charge injection and extraction on tree initiation in polyethylene. *IEEE T Power Ap Syst* 1978, **PAS-97**: 1749–1759.
[125] Neudeck PG, Okojie RS, Chen LY. High-temperature electronics—A role for wide bandgap semiconductors? *Proc IEEE* 2002, **90**: 1065–1076.
[126] Dyalsingh HM, Kakalios J. Thermopower and conductivity activation energies in hydrogenated amorphous silicon. *Phys Rev B* 1996, **54**: 7630–7633.
[127] Li F, Jiang T, Zhai JW, *et al*. Exploring novel bismuth-based materials for energy storage applications. *J Mater Chem C* 2018, **6**: 7976–7981.
[128] Huang W, Chen Y, Li X, *et al*. Ultrahigh recoverable energy storage density and efficiency in barium strontium titanate-based lead-free relaxor ferroelectric ceramics. *Appl Phys Lett* 2018, **113**: 203902.
[129] Yang HB, Yan F, Lin Y, *et al*. Enhanced recoverable energy storage density and high efficiency of $SrTiO_3$-based lead-free ceramics. *Appl Phys Lett* 2017, **111**: 253903.
[130] Yang HG, Qi H, Zuo RZ. Enhanced breakdown strength and energy storage density in a new $BiFeO_3$-based ternary lead-free relaxor ferroelectric ceramic. *J Eur Ceram Soc* 2019, **39**: 2673–2679.
[131] Dai ZH, Li DY, Zhou ZJ, *et al*. A strategy for high performance of energy storage and transparency in KNN-based ferroelectric ceramics. *Chem Eng J* 2022, **427**: 131959.
[132] Wang T, Jin L, Li CC, *et al*. Relaxor ferroelectric $BaTiO_3$–$Bi(Mg_{2/3}Nb_{1/3})O_3$ ceramics for energy storage application. *J Am Ceram Soc* 2015, **98**: 559–566.
[133] Xiong B, Hao H, Zhang SJ, *et al*. Structure, dielectric properties and temperature stability of $BaTiO_3$–$Bi(Mg_{1/2}Ti_{1/2})O_3$ perovskite solid solutions. *J Am Ceram Soc* 2011, **94**: 3412–3417.
[134] Wu LW, Wang XH, Li LT. Lead-free $BaTiO_3$–$Bi(Zn_{2/3}Nb_{1/3})O_3$ weakly coupled relaxor ferroelectric materials for energy storage. *RSC Adv* 2016, **6**: 14273–14282.
[135] Hu QY, Jin L, Wang T, *et al*. Dielectric and temperature stable energy storage properties of $0.88BaTiO_3$–$0.12Bi(Mg_{1/2}Ti_{1/2})O_3$ bulk ceramics. *J Alloys Compd* 2015, **640**: 416–420.
[136] Kong X, Yang LT, Cheng ZX, *et al*. Bi-modified $SrTiO_3$-based ceramics for high-temperature energy storage applications. *J Am Ceram Soc* 2020, **103**: 1722–1731.
[137] Zhou MX, Liang RH, Zhou ZY, *et al*. Combining high energy efficiency and fast charge–discharge capability in novel $BaTiO_3$-based relaxor ferroelectric ceramic for energy-storage. *Ceram Int* 2019, **45**: 3582–3590.
[138] Li WB, Zhou D, Liu WF, *et al*. High-temperature $BaTiO_3$-based ternary dielectric multilayers for energy storage applications with high efficiency. *Chem Eng J* 2021, **414**: 128760.
[139] Dai ZH, Xie JL, Liu WG, *et al*. Effective strategy to achieve excellent energy storage properties in lead-free $BaTiO_3$-based bulk ceramics. *ACS Appl Mater Interfaces* 2020, **12**: 30289–30296.
[140] Hu QY, Tian Y, Zhu QS, *et al*. Achieve ultrahigh energy storage performance in $BaTiO_3$–$Bi(Mg_{1/2}Ti_{1/2})O_3$ relaxor ferroelectric ceramics via nano-scale polarization mismatch and reconstruction. *Nano Energy* 2020, **67**: 104264.
[141] Ji SS, Li QJ, Wang DD, *et al*. Enhanced energy storage performance and thermal stability in relaxor ferroelectric $(1-x)BiFeO_3$–$x(0.85BaTiO_3$–$0.15Bi(Sn_{0.5}Zn_{0.5})O_3)$ ceramics. *J Am Ceram Soc* 2021, **104**: 2646–2654.
[142] Zhao L, Gao J, Liu Q, *et al*. Silver niobate lead-free antiferroelectric ceramics: Enhancing energy storage density by B-site doping. *ACS Appl Mater Interfaces* 2018, **10**: 819–826.
[143] Sa TL, Qin N, Yang GW, *et al*. W-doping induced antiferroelectric to ferroelectric phase transition in $PbZrO_3$ thin films prepared by chemical solution deposition. *Appl Phys Lett* 2013, **102**: 172906.
[144] Wang ZP, Zhang LX, Kang RR, *et al*. $(Bi_{0.5}Na_{0.5})TiO_3$-based relaxor ferroelectrics with enhanced energy-storage density and efficiency under low/moderate-fields via average ionic polarizability design. *Chem Eng J* 2022, **431**: 133716.
[145] Gao YF, Zhu XP, Yang B, *et al*. Grain size modulated $(Na_{0.5}Bi_{0.5})_{0.65}Sr_{0.35}TiO_3$-based ceramics with enhanced energy storage properties. *Chem Eng J* 2022, **433**: 133584.
[146] Zhang M, Yang HB, Li D, *et al*. Excellent energy density and power density achieved in $K_{0.5}Na_{0.5}NbO_3$-based ceramics with high optical transparency. *J Alloys Compd* 2020, **829**: 154565.
[147] Prakash D, Sharma BP, Rama Mohan TR, *et al*. Flux additions in barium titanate: Overview and prospects. *J Solid State Chem* 2000, **155**: 86–95.
[148] Wu T, Pu YP, Chen K. Dielectric relaxation behavior and energy storage properties in $Ba_{0.4}Sr_{0.6}Zr_{0.15}Ti_{0.85}O_3$ ceramics with glass additives. *Ceram Int* 2013, **39**: 6787–6793.
[149] Wu LW, Wang XH, Gong HL, *et al*. Core–satellite $BaTiO_3$@$SrTiO_3$ assemblies for a local compositionally graded relaxor ferroelectric capacitor with enhanced energy storage density and high energy efficiency. *J Mater Chem C* 2015, **3**: 750–758.
[150] Lee HY, Cho KH, Nam HD. Grain size and temperature dependence of electrical breakdown in $BaTiO_3$ ceramic. *Ferroelectrics* 2006, **334**: 165–169.
[151] Wang HY, Cao MH, Tao C, *et al*. Tuning the microstructure of $BaTiO_3$@FeO core–shell nanoparticles with low temperatures sintering dense nanocrystalline ceramics for high energy storage capability and stability. *J Alloys Compd* 2021, **864**: 158644.
[152] Wang HY, Cao MH, Huang R, *et al*. Preparation of $BaTiO_3$@NiO core–shell nanoparticles with antiferroelectric-

like characteristic and high energy storage capability. *J Eur Ceram Soc* 2021, **41**: 4129–4137.

[153] Chen LL, Wang HX, Zhao PY, *et al*. High permittivity and excellent high-temperature energy storage properties of X9R $BaTiO_3$–$(Bi_{0.5}Na_{0.5})TiO_3$ ceramics. *J Am Ceram Soc* 2020, **103**: 1113–1120.

[154] Zhang XT, Zhao LL, Liu LW, *et al*. Interface and defect modulation via a core–shell design in $(Na_{0.5}Bi_{0.5}TiO_3@La_2O_3)$–$(SrSn_{0.2}Ti_{0.8}O_3@La_2O_3)$–$Bi_2O_3$–$B_2O_3$–$SiO_2$ composite ceramics for wide-temperature energy storage capacitors. *Chem Eng J* 2022, **435**: 135061.

[155] Wu YC, Fan YZ, Liu NT, *et al*. Enhanced energy storage properties in sodium bismuth titanate-based ceramics for dielectric capacitor applications. *J Mater Chem C* 2019, **7**: 6222–6230.

[156] Xie JY, Yao MW, Gao WB, *et al*. Ultrahigh breakdown strength and energy density in PLZST@PBSAZM antiferroelectric ceramics based on core–shell structure. *J Eur Ceram Soc* 2019, **39**: 1050–1056.

[157] Bian F, Yan SG, Xu CH, *et al*. Enhanced breakdown strength and energy density of antiferroelectric Pb,La $(Zr,Sn,Ti)O_3$ ceramic by forming core–shell structure. *J Eur Ceram Soc* 2018, **38**: 3170–3176.

[158] Chu BJ, Lin MR, Neese B, *et al*. Large enhancement in polarization response and energy density of poly (vinylidene fluoride–trifluoroethylene–chlorofluoroethylene) by interface effect in nanocomposites. *Appl Phys Lett* 2007, **91**: 122909.

[159] Song Z, Liu HX, Hao H, *et al*. The effect of grain boundary on the energy storage properties of $(Ba_{0.4}Sr_{0.6M})TiO_3$ paraelectric ceramics by varying grain sizes. *IEEE T Ultrason Ferr* 2015, **62**: 609–616.

[160] Tunkasiri T, Rujijanagul G. Dielectric strength of fine grained barium titanate ceramics. *J Mater Sci Lett* 1996, **15**: 1767–1769.

[161] Beauchamp EK. Effect of microstructure on pulse electrical strength of MgO. *J Am Ceram Soc* 1971, **54**: 484–487.

[162] Liebault J, Vallayer J, Goueriot D, *et al*. How the trapping of charges can explain the dielectric breakdown performance of alumina ceramics. *J Eur Ceram Soc* 2001, **21**: 389–397.

[163] Chen IW, Wang XH. Sintering dense nanocrystalline ceramics without final-stage grain growth. *Nature* 2000, **404**: 168–171.

[164] Wang XZ, Huan Y, Zhao PY, *et al*. Optimizing the grain size and grain boundary morphology of $(K,Na)NbO_3$-based ceramics: Paving the way for ultrahigh energy storage capacitors. *J Materiomics* 2021, **7**: 780–789.

[165] Yang ZT, Du HL, Jin L, *et al*. A new family of sodium niobate-based dielectrics for electrical energy storage applications. *J Eur Ceram Soc* 2019, **39**: 2899–2907.

[166] Peng HF, Fan ZX, Liang YF, *et al*. Mechanochemical synthesis of superionic conducting materials. *Chin J Inorg Chem* 2006, **22**: 779–784. (in Chinese)

[167] Arlt G, Hennings D, de With G. Dielectric properties of fine-grained barium titanate ceramics. *J Appl Phys* 1985, **58**: 1619–1625.

[168] Li JM, Wang FF, Qin XM, *et al*. Large electrostrictive strain in lead-free $Bi_{0.5}Na_{0.5}TiO_3$–$BaTiO_3$–$KNbO_3$ ceramics. *Appl Phys A* 2011, **104**: 117–122.

[169] Tan SB, Liu EQ, Zhang QP, *et al*. Controlled hydrogenation of P(VDF-co-CTFE) to prepare P(VDF-co-TrFE-co-CTFE) in the presence of CuX (X = Cl, Br) complexes. *Chem Commun* 2011, **47**: 4544–4546.

[170] Xie AW, Qi H, Zuo RZ. Achieving remarkable amplification of energy-storage density in two-step sintered $NaNbO_3$–$SrTiO_3$ antiferroelectric capacitors through dual adjustment of local heterogeneity and grain scale. *ACS Appl Mater Interfaces* 2020, **12**: 19467–19475.

[171] Yan F, Bai HR, Ge GL, *et al*. Composition and structure optimized $BiFeO_3$–$SrTiO_3$ lead-free ceramics with ultrahigh energy storage performance. *Small* 2022, **18**: 2106515.

[172] Zhang L, Jiang SL, Fan BY, *et al*. Enhanced energy storage performance in $(Pb_{0.858}Ba_{0.1}La_{0.02}Y_{0.008})(Zr_{0.65}Sn_{0.3}Ti_{0.05})O_3$–$(Pb_{0.97}La_{0.02})(Zr_{0.9}Sn_{0.05}Ti_{0.05})O_3$ antiferroelectric composite ceramics by Spark Plasma Sintering. *J Alloys Compd* 2015, **622**: 162–165.

[173] Ceja-Cárdenas L, Lemus-Ruíz J, Jaramillo-Vigueras D, *et al*. Spark plasma sintering of α-Si_3N_4 ceramics with Al_2O_3 and Y_2O_3 as additives and its morphology transformation. *J Alloys Compd* 2010, **501**: 345–351.

[174] Shim SH, Yoon JW, Shim KB, *et al*. Low temperature synthesis of the microwave dielectric Bi_2O_3–MgO–Nb_2O_5 nano powders by metal–citrate method. *J Alloys Compd* 2006, **415**: 234–238.

[175] Zhang GZ, Zhu DY, Zhang XS, *et al*. High-energy storage performance of $(Pb_{0.87}Ba_{0.1}La_{0.02})(Zr_{0.68}Sn_{0.24}Ti_{0.08})O_3$ antiferroelectric ceramics fabricated by the hot-press sintering method. *J Am Ceram Soc* 2015, **98**: 1175–1181.

[176] Zhang GZ, Chen M, Fan BY, *et al*. High electrocaloric effect in hot-pressed $Pb_{0.85}La_{0.1}(Zr_{0.65}Ti_{0.35})O_3$ ceramics with a wide operating temperature range. *J Am Ceram Soc* 2017, **100**: 4581–4589.

[177] Li F, Hou X, Li TY, *et al*. Fine-grain induced outstanding energy storage performance in novel $Bi_{0.5}K_{0.5}TiO_3$–$Ba(Mg_{1/3}Nb_{2/3})O_3$ ceramics via a hot-pressing strategy. *J Mater Chem C* 2019, **7**: 12127–12138.

[178] Clavier N, Podor R, Dacheux N. Crystal chemistry of the monazite structure. *J Eur Ceram Soc* 2011, **31**: 941–976.

[179] Urek S, Drofenik M. The hydrothermal synthesis of $BaTiO_3$ fine particles from hydroxide–alkoxide precursors. *J Eur Ceram Soc* 1998, **18**: 279–286.

[180] Wang XC, Cai WQ, Xiao Z, *et al*. High energy-storage performance of lead-free $AgNbO_3$ antiferroelectric ceramics fabricated via a facile approach. *J Eur Ceram Soc* 2021, **41**: 5163–5169.

[181] Ren PR, Ren D, Sun L, *et al*. Grain size tailoring and enhanced energy storage properties of two-step sintered Nd^{3+}-doped $AgNbO_3$. *J Eur Ceram Soc* 2020, **40**: 4495–4502.

[182] Luo C, Zhu CH, Liang YH, *et al*. Promoting energy storage performance of $Sr_{0.7}Ba_{0.3}Nb_2O_6$ tetragonal tungsten bronze ceramic by a two-step sintering technique. *ACS Appl Electron Mater* 2022, **4**: 452–460.

[183] Jin Y, Wang JF, Jiang L, *et al*. Boosting up the capacitive energy storage performances of lead-free ceramics via grain engineering for pulse power applications. *Ceram Int* 2021, **47**: 2869–2873.

[184] Jain A, Wang YG, Guo H. Microstructure induced ultra-high energy storage density coupled with rapid discharge properties in lead-free $Ba_{0.9}Ca_{0.1}Ti_{0.9}Zr_{0.1}O_3$–$SrNb_2O_6$ ceramics. *Ceram Int* 2021, **47**: 487–499.

[185] Luo NN, Han K, Zhuo FP, *et al*. Design for high energy storage density and temperature-insensitive lead-free antiferroelectric ceramics. *J Mater Chem C* 2019, **7**: 4999–5008.

[186] Li Y, Liu Y, Tang MY, *et al*. Energy storage performance of $BaTiO_3$-based relaxor ferroelectric ceramics prepared through a two-step process. *Chem Eng J* 2021, **419**: 129673.

[187] Hong K, Lee TH, Suh JM, *et al*. Perspectives and challenges in multilayer ceramic capacitors for next generation electronics. *J Mate Chem C* 2019, **7**: 9782–9802.

[188] Wang HX, Zhao PY, Chen LL, *et al*. Energy storage properties of $0.87BaTiO_3$–$0.13Bi(Zn_{2/3}(Nb_{0.85}Ta_{0.15})_{1/3})O_3$ multilayer ceramic capacitors with thin dielectric layers. *J Adv Ceram* 2020, **9**: 292–302.

[189] Li F, Wang LH, Jin L, *et al*. Achieving single domain relaxor–PT crystals by high temperature poling. *CrystEngComm* 2014, **16**: 2892–2897.

[190] Li F, Jin L, Xu Z, *et al*. Electrostrictive effect in ferroelectrics: An alternative approach to improve piezoelectricity. *Appl Phys Rev* 2014, **1**: 011103.

[191] Chen LM, Sun NN, Li Y, *et al*. Multifunctional antiferroelectric MLCC with high-energy-storage properties and large field-induced strain. *J Am Ceram Soc* 2018, **101**: 2313–2320.

[192] Cai ZM, Wang HX, Zhao PY, *et al*. Significantly enhanced dielectric breakdown strength and energy density of multilayer ceramic capacitors with high efficiency by electrodes structure design. *Appl Phys Lett* 2019, **115**: 023901.

[193] Zhao PY, Wang HX, Wu LW, *et al*. High-performance relaxor ferroelectric materials for energy storage applications. *Adv Energy Mater* 2019, **9**: 1803048.

[194] Liu XH, Zhu JY, Li Y, *et al*. High-performance $PbZrO_3$-based antiferroelectric multilayer capacitors based on multiple enhancement strategy. *Chem Eng J* 2022, **446**: 136729.

[195] Cai ZM, Zhu CQ, Wang HX, *et al*. High-temperature lead-free multilayer ceramic capacitors with ultrahigh energy density and efficiency fabricated via two-step sintering. *J Mater Chem A* 2019, **7**: 14575–14582.

[196] Wang HX, Zeng CY, Liu BB, *et al*. Energy storage properties of surface-modified $BaTiO_3$ ceramic films for multilayer capacitors applications. *J Adv Dielectr* 2019, **9**: 1950027.

[197] Jiang SL, Zhang L, Zhang GZ, *et al*. Effect of Zr : Sn ratio in the lead lanthanum zirconate stannate titanate anti-ferroelectric ceramics on energy storage properties. *Ceram Int* 2013, **39**: 5571–5575.

[198] Xie AW, Zuo RZ, Qiao ZL, *et al*. $NaNbO_3$–$(Bi_{0.5}Li_{0.5})TiO_3$ lead-free relaxor ferroelectric capacitors with superior energy-storage performances via multiple synergistic design. *Adv Energy Mater* 2021, **11**: 2101378.

[199] hang L, Jiang SL, Zeng YK, *et al*. Y doping and grain size co-effects on the electrical energy storage performance of $(Pb_{0.87}Ba_{0.1}La_{0.02})(Zr_{0.65}Sn_{0.3}Ti_{0.05})O_3$ anti-ferroelectric ceramics. *Ceram Int* 2014, **40**: 5455–5460.

[200] Jiang ZH, Yang ZY, Yuan Y, *et al*. High energy storage properties and dielectric temperature stability of $(1-x)(0.8Bi_{0.5}Na_{0.5}TiO_3$–$0.2Ba_3Sr_{0.4}TiO_3)$–$xNaNbO_3$ lead-free ceramics. *J Alloys Compd* 2021, **851**: 156821.

[201] Han K, Luo NN, Mao SF, *et al*. Ultrahigh energy-storage density in A-/B-site co-doped $AgNbO_3$ lead-free antiferroelectric ceramics: Insight into the origin of antiferroelectricity. *J Mater Chem A* 2019, **7**: 26293–26301.

[202] Sun HN, Wang XJ, Sun QZ, *et al*. Large energy storage density in $BiFeO_3$–$BaTiO_3$–$AgNbO_3$ lead-free relaxor ceramics. *J Eur Ceram Soc* 2020, **40**: 2929–2935.

[203] Yan F, Shi YJ, Zhou XF, *et al*. Optimization of polarization and electric field of bismuth ferrite-based ceramics for capacitor applications. *Chem Eng J* 2021, **417**: 127945.

[204] Wang G, Lu ZL, Li JL, *et al*. Lead-free $(Ba,Sr)TiO_3$–$BiFeO_3$ based multilayer ceramic capacitors with high energy density. *J Eur Ceram Soc* 2020, **40**: 1779–1783.

[205] Zhao Y, Meng XJ, Hao XH. Synergistically achieving ultrahigh energy-storage density and efficiency in linear-like lead-based multilayer ceramic capacitor. *Scripta Mater* 2021, **195**: 113723.

[206] Chao WN, Yang TQ, Li YX. Achieving high energy efficiency and energy density in $PbHfO_3$-based antiferroelectric ceramics. *J Mater Chem C* 2020, **8**: 17016–17024.

[207] Zhang M, Yang HB, Yu YW, *et al*. Energy storage performance of $K_{0.5}Na_{0.5}NbO_3$-based ceramics modified by $Bi(Zn_{2/3}(Nb_{0.85}Ta_{0.15})_{1/3})O_3$. *Chem Eng J* 2021, **425**: 131465.

[208] Zuo CY, Yang SL, Cao ZQ, *et al*. Excellent energy storage and hardness performance of $Sr_{0.7}Bi_{0.2}TiO_3$ ceramics fabricated by solution combustion-synthesized nanopowders. *Chem Eng J* 2022, **442**: 136330.

[209] Zhang M, Yang HB, Li D, *et al*. Giant energy storage efficiency and high recoverable energy storage density achieved in $K_{0.5}Na_{0.5}NbO_3$–$Bi(Zn_{0.5}Zr_{0.5})O_3$ ceramics. *J Mater Chem C* 2020, **8**: 8777–8785.

[210] Sun CC, Chen XL, Shi JP, *et al*. Simultaneously with large energy density and high efficiency achieved in $NaNbO_3$-based relaxor ferroelectric ceramics. *J Eur Ceram Soc* 2021, **41**: 1891–1903.

[211] Zhou MX, Liang RH, Zhou ZY, *et al*. Superior energy

storage properties and excellent stability of novel $NaNbO_3$-based lead-free ceramics with A-site vacancy obtained via a Bi_2O_3 substitution strategy. *J Mater Chem A* 2018, **6**: 17896–17904.

[212] Li CW, Xiao YM, Fu TY, *et al*. High capacitive performance achieved in $NaNbO_3$-based ceramics via grain refinement and relaxation enhancement. *Energy Technol* 2022, **10**: 2100777.